

# Proton radiography with limited scattering angles: a Monte Carlo study

Bachelor thesis

J.R. de Jong

July 5, 2019

First examiner: dr. E.R. van der Graaf

Second examiner: dr. P.G. Dendooven

## Abstract

Proton therapy is a relatively novel cancer treatment technique that is often favoured if it is required that the healthy tissue that surrounds the tumour remains as undamaged as possible. A treatment plan can be determined by a combination of planning computed tomography and proton radiography. However, multiple Coulomb scattering inside the tissue causes proton radiography to be sensitive to uncertainties. In order to improve the accuracy of proton radiography, this study investigates the effect of the rejection of scattered protons by doing several Monte Carlo simulations. The accuracy of the corrected radiographs is shown to be improved for binning angles of 0.5, 0.75 and 1 degrees. By taking into account the contrast of the radiograph and the uncertainty in the data, the optimal binning angle is determined to be 0.75 degrees.



university of  
 groningen

faculty of science  
 and engineering

# Contents

<b>1</b>	<b>Introduction</b>	<b>2</b>
<b>2</b>	<b>Theory</b>	<b>2</b>
2.1	Proton interactions in matter . . . . .	3
2.1.1	Coulomb interactions . . . . .	3
2.1.2	Multiple Coulomb Scattering . . . . .	5
2.1.3	Nuclear Reactions . . . . .	6
2.2	Procedure for a proton treatment plan . . . . .	6
2.2.1	Planning CT scan . . . . .	6
2.2.2	Proton radiography . . . . .	7
2.2.3	The spread-out Bragg peak . . . . .	8
2.3	Creating a parallel proton beam . . . . .	8
<b>3</b>	<b>Monte Carlo simulations</b>	<b>9</b>
3.1	The principle behind the Monte Carlo Method . . . . .	9
3.2	Designing the MCNPX input code . . . . .	10
3.2.1	Basic geometric inputs . . . . .	10
3.2.2	Lattice based voxels . . . . .	11
3.2.3	Physical inputs . . . . .	12
3.3	Setup of the Monte Carlo simulation . . . . .	13
3.4	Combining the F2 and F6 tally . . . . .	16
<b>4</b>	<b>Results</b>	<b>16</b>
4.1	Radiographs of the averaged proton energy deposition . . . . .	16
4.2	Radiographs of the averaged proton flux . . . . .	18
4.3	Corrected radiographs of the averaged proton energy deposition . . . . .	21
<b>5</b>	<b>Discussion</b>	<b>23</b>
5.1	Accuracy of the radiographs . . . . .	23
5.2	Comparison with literature . . . . .	23
5.3	Optimal binning angle and further research . . . . .	24
<b>6</b>	<b>Conclusion</b>	<b>24</b>
	<b>Appendix A The complete MCNPX input code</b>	<b>26</b>
	<b>Appendix B MATLAB code to import the F2 tally with the experimental data</b>	<b>31</b>
	<b>Appendix C MATLAB code to import the F6 tally</b>	<b>33</b>

# 1 Introduction

The interest of cancer treatment using proton therapy is steadily growing ever since the 1990s [1]. Proton therapy is an addition to radiation techniques that use photons to penetrate the human tissue. Both treatment methods are capable of applying sufficient damage to a tumour in order to cure a patient, however protons can very effectively release their energy precisely at a specific location in the body so that the damage on the healthy tissue before and after the tumour can be kept very low. This is the motivation that proton therapy is often favoured over other treatments, especially if it is applied in parts of the human body that have a complex geometry, which for example is the case in the head and neck region.

For proton therapy it is very important that the proton range in the tissue can be determined very accurately. In order to calculate the range, the stopping power is needed. This is the amount of energy that is deposited to a medium in a certain length. Often, the relative stopping power (RSP) is used, which is the stopping power relative to the stopping power in water. Computed tomography (CT) is a technique that is currently used to indirectly determine these quantities [2]. It uses photons to visualize the problem region in the body and calculates the linear attenuation coefficient of every voxel. In order to determine the RSP from the obtained CT data, a conversion is needed. Because this conversion involves two particles of completely different nature, this method to predict the RSP is sensitive to uncertainties.

To more accurately predict the proton range, the CT method can be combined with another technique called proton radiography. For this technique a scintillation screen is placed in such a way that the tissue lies in between the proton source and the screen. In comparison with proton therapy higher proton energies are needed for proton radiography, because the protons have to travel through the body to be able to be detected by the screen. The CT technique determines the proton stopping power of the tissue so that the proton energy at the position of the screen can be calculated. The proton energy is also measured by use of the scintillation screen, i.e. by proton radiography. The predicted proton energy from the CT scan is then compared with the measured energy from the proton radiograph. If there is a large dissimilarity between the results, the CT data can be adapted in such a way that the difference between the data sets is minimized. In this way proton radiography helps to improve the accuracy of the CT data by using it before treatment as a CT verification. As a result, the proton range can be predicted more accurately.

However, a disturbing effect arises when using proton radiography and hence the treatment procedure explained above has to be slightly altered. Especially in dense materials like bone, the probability of protons to interact elastically with heavy atomic nuclei becomes of significant magnitude [3]. This phenomenon is called multiple Coulomb scattering and leads to the deflection of protons inside the human body. Because of the fact that proton radiography is a two-dimensional imaging system, protons that move straight ahead can not be distinguished from protons that travel in a deflected way. This means that if there is no correction for multiple Coulomb scattering, the data of the radiograph can not be directly converted to the energy loss of the proton. The uncertainty of the proton radiograph can thus be improved by letting it consist of only protons that are travelling in a straight line. Hence, a correction is needed for protons that have scattered significantly in the tissue.

For this purpose, in this report a Monte Carlo code has been extended in order to simulate the energy deposition of protons in a scintillation screen, which has been mimicked by a lattice-based tally in order to run the simulation more efficiently [4]. Monte Carlo simulations have been done using a highly simplified tissue that is placed in between the proton source and the scintillation screen. In the simulations there is accounted for multiple Coulomb scattering. The simulations have been compared with a few data sets of an experiment that has been previously done at KVI-CART [5]. By looking at the effect of multiple Coulomb scattering on the radiograph in the simulations, the data of the radiographs obtained in the experiment can be adapted and thus improved.

## 2 Theory

In order to take full advantage of the improvements that proton radiography may have on treatment planning, it is crucial to understand some basic concepts of proton behaviour in matter. In

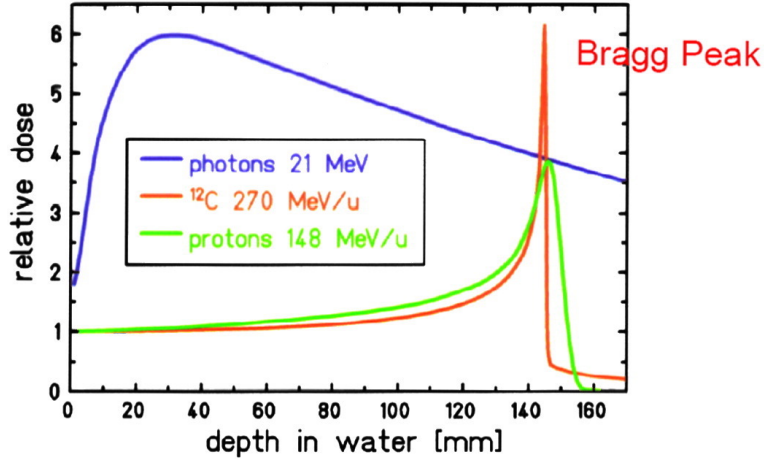


Figure 1: The relative dose versus the water depth for photons, carbon ions and protons [6].

this section the relevant proton interactions are discussed and a short description is given of the mechanisms behind CT imaging and proton radiography.

## 2.1 Proton interactions in matter

When protons travel through human tissue they mainly interact with other charged particles via Coulomb interactions, for instance with electrons and atomic nuclei. Electrons hardly influence the proton direction, however significant deflection can occur if the proton encounters an atomic nucleus. In the latter case the proton interacts elastically, i.e. it scatters. This is due to the fact that protons are heavy compared to electrons but light compared to atomic nuclei. Especially in dense materials that consist of many heavy atomic nuclei, it is more probable for deflections to occur so that multiple Coulomb scattering happens more often. Alternatively, it can happen that protons interact inelastically with atomic nuclei, so that the proton is fused together with the atomic nuclei. This can lead to the production of various kinds of other particles.

### 2.1.1 Coulomb interactions

Proton therapy relies on the fact that protons are decelerated in a special way when travelling through a material, for example a human tissue. From the moment the proton enters the tissue it first slowly loses its energy. At a certain distance from the front surface of the tissue the energy loss increases very rapidly until it decreases again very abruptly. This behaviour is shown in figure 1 for protons that are travelling through water. The largest part of the proton energy is released at a very specific range, so that there is a small region of very high energy deposition. This peak in the dose delivery that occurs around this range is called the Bragg peak. A graph of the relative dose to water by carbon ions is also included in figure 1. It can be seen that carbon ions show even a sharper Bragg peak and that the dose that is deposited to the healthy tissue is slightly lower. Because of this reason, heavy ions can also be used for cancer treatments. However, this report specifically considers proton therapy and thus features of therapies with heavy ions are not discussed.

In order to compare the energy deposition of protons with that of photons, the behaviour of the latter particle is shown in the same figure. A major difference between the two energy depositions is that a large part of the photon energy is already absorbed close to the front surface of the tissue, whilst the majority of the protons has still not deposited a significant amount of energy there. This is because of the exponential decrease of the photon energy deposition. Photons can not very accurately release their energy at a specific location and so do not have a narrow region where there is peak in the dose delivery, i.e. photons do not have a Bragg peak. In practice however, a tumor is irradiated from multiple directions so that the dose delivery at the tumour accumulates

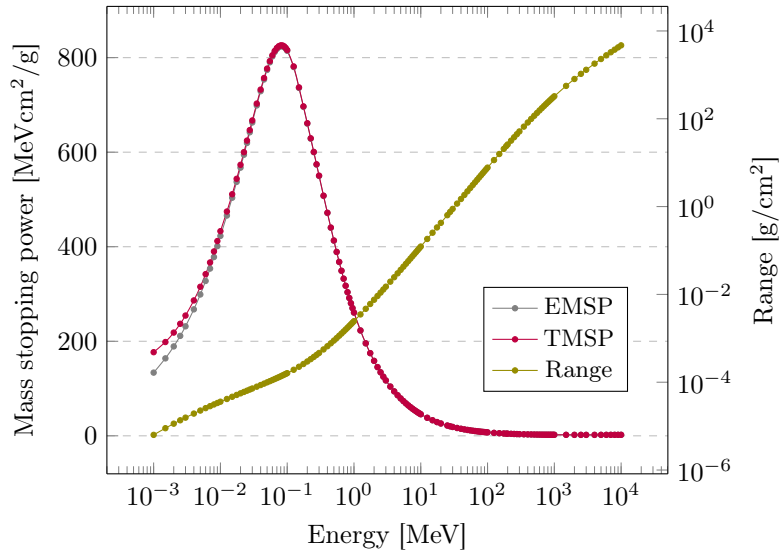


Figure 2: The electronic mass stopping power (EMSP), the total mass stopping power (TMSP) and range versus the energy for a proton that is travelling through water. The data is calculated using the pSTAR program [7].

for both proton and photon treatments. Proton therapy is favoured over photon irradiation if it is important that the healthy tissue needs to stay as undamaged as possible. For instance, healthy tissue of children is preferably kept undamaged to prevent the formation of secondary tumours at a later age. Proton therapy is also favoured if a tumour is located in the vicinity of important organs or in the head and neck region of the body.

The major purpose of proton therapy is to deliver the protons in the correct region in the tissue, precisely at the tumour. By varying the initial proton energy, the position of the Bragg peak can be adjusted so that it will lie in the tumour region. To do this properly, you need to know the proton energy deposition in the tissue, which is often called the proton stopping power. Formally, the stopping power  $S$  of a particle is the amount of energy that has been deposited to a medium in a certain length and is often denoted as  $dE/dx$ . It is convenient to divide the stopping power by the density of the medium to obtain the mass stopping power, because this quantity is almost independent of the characteristics of the medium. In this way, mass stopping powers can be more easily compared to stopping powers of other media. The proton energy deposition inside a medium can be described by the Bethe-Bloch equation [8] which is given by

$$S = -\frac{dE}{dx} = \frac{4\pi n}{m_e c^2} \frac{z^2}{\beta^2} \left(\frac{e^2}{4\pi\epsilon_0}\right)^2 \left[ \ln\left(\frac{2m_e c^2 \beta^2}{I(Z) \cdot (1 - \beta^2)}\right) - \beta^2 \right] \quad (1)$$

where  $e$  and  $m_e$  are the electronic charge and mass, respectively.  $\epsilon_0$  is the vacuum permittivity and is equal to  $8.854 \times 10^{-12} \frac{F}{m}$ . A proton with charge  $z$  and velocity  $\beta$  with respect to the speed of light  $c$  travels through the medium that has an electron density  $n$  that is given by

$$n = \frac{N_A}{M_u} \frac{Z\rho}{A} \quad (2)$$

$Z$ ,  $A$  and  $\rho$  are the atomic number, the relative atomic mass number and the density of the medium, respectively.  $N_A$  is the Avogadro number and  $M_u$  is the molar mass constant. Equation 1 can be divided by the density of the medium to obtain the mass stopping power. The mass stopping power versus the energy is plotted in figure 2 for protons that are travelling through water. Water is frequently used as an approximation to human tissue because of its comparable density. As can be seen in figure 2, the stopping power is low for high energies and increases for lower energies. After the mass stopping power has reached a maximum it decreases again for lower energies.

When the proton enters the tissue it has a relatively high energy so that it has a low stopping power, as can be seen from figure 2. Since the proton is charged it interacts with other charged particles inside the tissue. Two main contributions cause the proton to decelerate of which the greatest is due to atomic electrons in the tissue. Electrons are responsible for the electronic stopping power of the proton, which is described by the Bethe-Bloch equation. The proton and electron are being attracted to each other by the Coulomb force so that both particles collide. The proton transfers a part of its energy to the electron which leads to an excitation of the corresponding atom inside the tissue. In this way, the Coulomb force leads to a slow decrease in the proton energy. This process continues and thus the proton energy decreases further. As a consequence the proton stopping power is increasing accordingly because of the specific  $\beta$ -dependence in equation 1. At very low kinetic energies, the cross section of the elastic interaction between the proton and the atomic nucleus inside the tissue increases [9]. From this point the nuclear stopping power becomes non-negligible.

If it is assumed that only the electronic and nuclear stopping power contribute in the deceleration process of the proton in the tissue, the total stopping power can be calculated by adding the two contributions together [10] so that

$$S = S_e + S_n \quad (3)$$

where  $S_e$  and  $S_n$  are the electronic and nuclear stopping power, respectively. The electronic stopping power  $S_e$  in equation 3 is equal to the stopping power  $S$  in equation 1. In figure 2 the electronic mass stopping power is also shown. It can be seen that for protons in water the nuclear stopping power becomes non-negligible for very low energies. However, it is still not of significant magnitude. The nuclear stopping power thus has only to be considered at the very last stage of the proton deceleration process. However, if heavier ions are used for a cancer treatment, the nuclear stopping power may dominate over the electronic stopping power at some point. It is thus an important contribution to consider.

In the present study, protons with initial kinetic energies of approximately 190 MeV have been used so that relativistic effects have to be taken into account. Multiple corrections can be added to equation 1, especially improving the results for very low and high energies [11]. However, they are beyond the scope of this report and therefore not discussed in more detail.

The concept that is most crucial for proton treatment is the proton range. It is this quantity that needs to be predicted very accurately in order for the treatment to be successful. If it is assumed that protons are hardly scattered laterally, i.e. perpendicular to the initial direction, the protons travel in a straight line so that the proton range  $R_p$  [12] can be estimated by

$$R_p = \int_0^{E_0} \frac{1}{S} dE \quad (4)$$

where  $E_0$  is the initial proton energy and  $S$  is the total stopping power from formula 3. From equation 4 it is clear that the proton range depends on the initial proton energy and it is increasing for higher energies. This behaviour is plotted in figure 2, in which the proton range is given in units of  $\text{g}/\text{cm}^2$  because the range is obtained using the mass stopping power. The assumption to neglect proton scattering turns out to be valid for materials with a low atomic number. However, the lateral deflection of protons becomes significant for materials of higher atomic number [8], a relevant example is human bone. Therefore, during a treatment it is more accurate to use a corrected version of equation 4, however this is not discussed in more detail.

### 2.1.2 Multiple Coulomb Scattering

If protons traverse through a material there is a probability to interact elastically with the atomic nuclei inside the material. It is very likely for a proton to change direction after interacting with an atomic nucleus, because (except for the hydrogen atom) protons have a lower mass than atomic nuclei. When there are multiple of these elastic scattering events in the tissue, the effect is called multiple Coulomb scattering [13]. The number of scattering events depends on the thickness and density of the material, because these determine the total number of scattering centers that are contained inside the tissue.

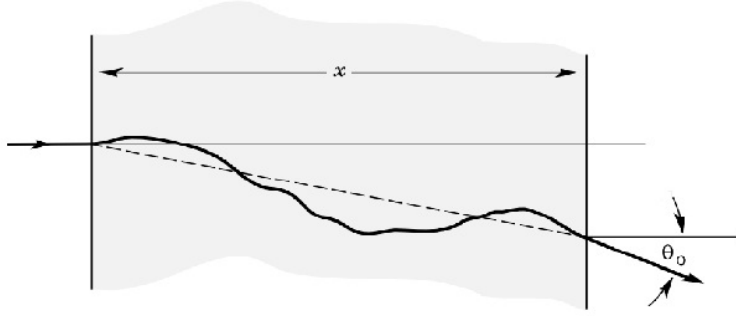


Figure 3: The trajectory of a proton that travels through a medium of thickness  $x$ . It is deflected by multiple Coulomb scattering [17] and leaves the material with an angle of  $\theta_0$  with respect to the initial direction.

Because of multiple Coulomb scattering, protons are deflected and their trajectory starts to deviate from their original path, which is shown in figure 3. Protons gain a lateral deflection and thus leave the tissue of thickness  $x$  at a position with a certain lateral displacement from the original path. The mean squared of the angular deflection  $\theta_0$  with respect to the initial direction of the proton [14] can be described by

$$\langle \theta_0^2 \rangle \propto \frac{\rho \cdot x}{(pv)^2} \frac{Z^2 z^2}{A} \quad (5)$$

$Z$ ,  $A$  and  $\rho$  respectively are the atomic number, the relative atomic mass number and the density of the medium, as previously defined. The proton has a charge  $z$ , a momentum  $p$  and a velocity  $v$ . As can be seen from equation 5, the effective scattering angle increases for lower proton energies. Also note that the scattering angle strongly depends on the atomic number and the material density.

It turns out that the angular distribution of the protons can be approximated by a Gaussian fit if large angles of  $\theta_0$  are not considered [15]. Also, there seems to be a correlation between the lateral displacement and the outgoing angle of the proton, namely that the outgoing angle gets larger for a larger lateral displacement [16]. In this report, data of scattered protons has been obtained by a Monte Carlo simulation and no further analytical calculations have been done on multiple Coulomb scattering. Therefore, the theory behind multiple Coulomb scattering is not discussed more extensively.

### 2.1.3 Nuclear Reactions

Protons not only interact elastically but can also interact non-elastically with atomic nuclei. In the latter case, the proton and atomic nucleus collide so that a nuclear reaction occurs. Depending on the initial proton energy, a multitude of different secondary particles can be formed. The most probable to form are protons, deuterons, tritons,  $^3\text{He}$ ,  $^4\text{He}$ , photons and neutrons. For the purpose of this report nuclear interactions are not discussed in further detail. However, all simulations take into account the creation of the particles that have been mentioned.

## 2.2 Procedure for a proton treatment plan

### 2.2.1 Planning CT scan

A so called planning CT scan is made before the cancer treatment with the purpose to predict the proton stopping power of every voxel as accurate as possible. A voxel is a small 3-dimensional volume that forms the fundamental building block of the problem region in the body. If the size of the voxel is made smaller, this region can be described more accurately. The planning CT scan uses photons from an X-ray tube to obtain the linear attenuation coefficient  $\mu$  of every voxel. The linear attenuation coefficient is a quantity that describes to which extent the photons are attenuated throughout the tissue.

In order to determine the proton stopping power of every voxel from the linear attenuation coefficient that has been obtained from the planning CT scan, some specifications of the tissue have to be known. From equation 1 and 2 it can be seen that the effective atomic number  $Z$  of the tissue, the mean excitation potential  $I(Z)$  and the electron density are unknown quantities that characterize the medium. Because the mean excitation potential depends on the effective atomic number, the proton stopping power can be determined from the planning CT by the effective atomic number and the electron density of the tissue. The linear attenuation coefficient is a function of both quantities [18] and obeys

$$\mu(E) = \rho_e \sigma_e(Z, E) \quad (6)$$

However, equation 6 can not be solved because both the electron density and the effective atomic number of the tissue are unknown. A second independent equation that has the form of equation 6 can be obtained by extending the CT apparatus to a dual energy CT (DECT) imaging system. This means that the X-ray tube makes a second scan at a different voltage, that results in an X-ray photon spectrum with a different energy. In this way, two independent equations are obtained that can thus be solved for both the electron density and the effect atomic number. The proton stopping power can subsequently be determined from the obtained quantities. The accuracy can be further improved if the CT technique is combined with a method that gives the proton stopping power directly and thus does not need any difficult conversion. Proton radiography is a technique that can help to improve the determination of the proton stopping power of every voxel in the tissue by combining it with CT imaging. It is important to realize that proton radiography can thus not be used as a treatment on its own.

### 2.2.2 Proton radiography

The basic principle for making a radiograph is shown in figure 4, which is not drawn to scale. Firstly, a planning CT image of the problem region in the body has been made so that the linear attenuation coefficient of every voxel is known. This is then converted to the proton stopping power for every voxel in the way that has been described earlier. Protons that have significantly scattered have traversed a path that is not precisely known, because of the probabilistic nature of multiple Coulomb scattering. Because scattered protons do not traverse the body in a straight line, the total energy loss of the scattered protons in the body can not be determined accurately. For protons that are travelling in a straight line and traverse the entire tissue, the stopping power in each voxel can be used to calculate the total energy loss  $dE$ . In this way the final proton energy can be predicted from the CT image based stopping powers. A proton radiograph is being made so that the measurements of the proton energy  $E_p$  from the scintillation screen can be compared with the prediction of the CT method. The largest accuracy in the proton stopping power is achieved

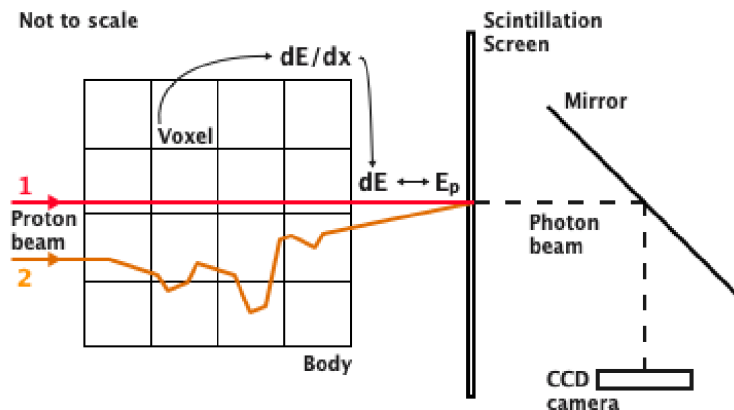


Figure 4: The basic principle of a setup to obtain a proton radiograph, which is not drawn to scale. A proton beam irradiates a human body that consists of voxels. From a planning CT scan, the energy loss  $dE$  is determined and compared with the proton energy  $E_p$  that is measured by a scintillation screen.

if the difference between the CT prediction and the measurement of the radiograph is minimized. This can be done by adapting the CT data until a minimum difference is obtained. A scintillation screen is being used for the proton detection to make the proton radiograph. If a proton enters the scintillating material, the material gets excited because some energy from the proton is transferred to the screen. The absorbed energy is re-emitted as light. The light is reflected by a mirror and collected at a different screen where it is detected by a CCD camera. As can be seen from equation 1, a low energetic proton has a large stopping power. This means that a lot of energy is deposited at the scintillation screen, which results in the re-emission of that same amount of energy. Therefore, a low energetic proton gives rise to a bright spot at the radiograph. Before hitting the scintillation screen, protons may have travelled through other materials. If a material is dense and thus harder to travel through, more energy is deposited in that material and therefore a low energetic proton leaves the material. Hence, a bright spot at the radiograph can be linked to a proton that travelled through a material of high density.

A drawback of proton radiography is the fact that it can not distinguish between scattered particles and particles that have not deflected, as is also shown in figure 4. Proton 1 is not deflected during its path and ends up at the same point as proton 2, whilst proton 2 is deflected by multiple Coulomb scattering. In this report, all protons that have deflected considerably have been rejected from the data sets of the simulation, so that a radiograph of higher accuracy is obtained. The rejection of scattered protons will be more extensively discussed in the section about Monte Carlo simulations.

### 2.2.3 The spread-out Bragg peak

In the previous section all elements that are needed to understand the basic principles of cancer treatment using proton therapy have been discussed. However in practice, treatments often differ in complexity. As mentioned before, the largest fraction of the total proton energy is released to a small region in the tissue. This makes sure that only a small part of the tissue is irradiated and that healthy tissue stays undamaged. However, in many cases the width of the Bragg peak is smaller than the width of the tumour. Therefore, treatments often use protons of multiple energies to obtain a spread-out Bragg peak (SOBP). In figure 5 pristine Bragg peaks are shown for multiple proton energies. As can be seen in the figure, the entire tumour region has been covered by a significant amount of dose by irradiating the tissue with protons of multiple energies. At the same time, the dose in the healthy tissue is kept relatively low. The dose distribution of the X-ray beam is shown as comparison.

## 2.3 Creating a parallel proton beam

In practice, a cancer treatment is being done with protons of multiple energies which makes it more difficult to produce the protons. Most of the time a cyclotron [20] is used to accelerate the protons. However, this type of accelerator can only produce a mono-energetic beam. Different energies have thus to be produced by a set of degraders. A degrader is a thin metal plate that is placed between the source and the patient. When the protons pass through the degrader they deposit a part of their energy to the degrader so that they decelerate. By using multiple degraders of various thicknesses, a set of different proton energies can be obtained. By using a disk that is made up of different segments that each contains a degrader of a different thickness [21], multiple energetic protons can be produced during a treatment by rotating the disk. Sometimes, instead of a cyclotron a synchrotron is used. This type of accelerator can produce multiple energetic protons by modifying the electric and magnetic field strength inside the accelerator.

An exit foil [22] is used at the end of the accelerator so that the inner region of the accelerator is closed and that a vacuum can be maintained inside the accelerator. A scatter foil is used to increase the width of the proton beam. After the foil, the protons do not travel parallel to the initial direction anymore. However, in order to obtain a constant proton flux over the entire width of the body, it is important for the proton beam to become parallel again. Therefore, collimators are placed between the scatter foil and the scintillation screen. Collimators are hollow cylinders that block protons with large scattering angles. In this way, only protons that travel parallel to the initial direction are allowed to traverse towards the body. The width of the proton beam can

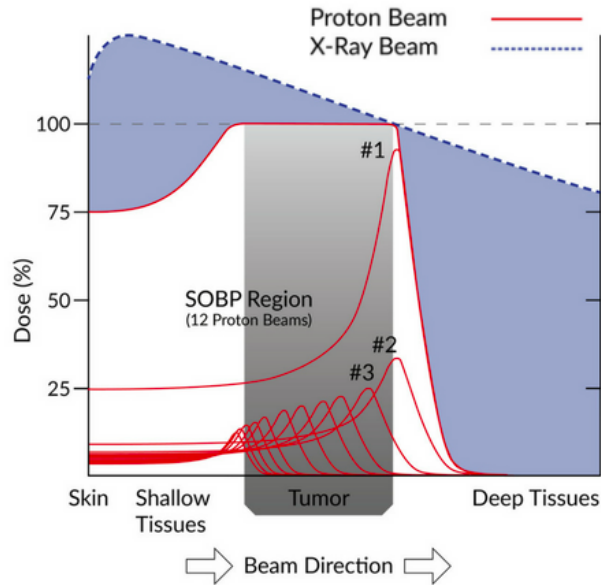


Figure 5: The relative dose versus the range for protons and photons to show how a spread-out Bragg peak (SOBP) is obtained using irradiation by multiple energetic protons (#1,#2,#3,...) [19]. The photon dose is shown as comparison.

be adjusted by changing the diameter of the aperture of the collimator. For a fixed aperture, the proton beam becomes more parallel if the collimator is placed closer to the body, i.e. at a larger distance from the scatter foil. However, the number of protons that traverse the collimator with respect to the total number of protons that are created at the source must also be taken into account when placing the collimator. Namely, this relative proton flux decreases if the distance between the scatter foil and the collimator increases. Therefore, the collimator must be placed at a position at which the proton beam is sufficiently parallel and at which the proton flux is still sufficiently high.

### 3 Monte Carlo simulations

A Monte Carlo code was extended in order to simulate the proton energy deposition in a scintillation screen. The data obtained by the simulation distinguished between scattered protons and protons that were not scattered. For all simulations the Monte Carlo N-Particle eXtended (MCNPX) 2.7.0. code had been used [23]. This code has been designed for simulating nuclear processes and so is widely applicable over a whole spectrum of areas. MCNPX can practically track all particles and more than 2000 heavy ions over a very large particle energy range [24].

#### 3.1 The principle behind the Monte Carlo Method

Monte Carlo simulations are often used for problems that are difficult to solve analytically. The Monte Carlo method is based on randomness and thus does not solve any explicit equation. A sequence of numbers that is made by a computer can never be 'true' random because in all cases a certain algorithm has to be involved. By developing an algorithm that is repeating after a vast amount of numbers, it may be approximated to be a random sequence. For this purpose, the Monte Carlo method uses a pseudo-random generator [25], i.e. a code that tries to generate a sequence of numbers that is approximated to be truly random by making the period of the sequence very large. In order to start the Monte Carlo simulation, a so called seed (a number) has to be given as an input. The simulation only gives a different result if a different seed is used. The pseudo-random number generator produces numbers that lie between 0 and 1 and should be equally distributed in

this domain for the Monte Carlo method to be accurate. The Monte Carlo estimation gets more accurate and reaches the correct result more precisely if more simulations are being done.

Let's consider a proton interaction with an electron (A), a proton scattering by an atomic nucleus (B) and the production of a secondary neutron by a nuclear reaction (C). Assume that the probabilities of interactions A, B and C are 0.7, 0.2 and 0.1, respectively. The Monte Carlo code is designed in such a way that each generated random number is labelled to a certain interaction process [26]. Using this principle, interaction A occurs if the generated random number lies between 0 and 0.7, interaction B occurs if it lies between 0.7 and 0.9 and interaction C occurs if it lies between 0.9 and 1. A better accuracy of the Monte Carlo method is achieved for an increased amount of random numbers.

Once a particle is created in MCNPX, it is followed until it is not adding more information to the problem. A particle can for instance escape to a region that has been assigned as unimportant or it may disappear by decay or in a nuclear reaction. MCNPX also takes interaction processes into account that are less probable, for example proton bremsstrahlung. Interaction processes that are relevant for secondary particles like electrons are also considered in the simulations. However, the discussion of particle interactions in this report is kept basic and thus only the most probable proton interactions have been mentioned.

## 3.2 Designing the MCNPX input code

The general structure of the MCNPX input code consists of a block with cell cards, surface cards and data cards. A blank line distinguishes between each block. The cell and surface cards are used to describe the geometry of the problem and the data cards are needed to describe all physical quantities of the system. Information from the simulation is only acquired if this is explicitly written in the code and a so called tally card has been specified. In this section, an explanation is given about designing the problem geometry in MCNPX, while focusing on the use of lattices in combination with F2 and F6 tallies. The source specification and material composition are also shortly discussed.

### 3.2.1 Basic geometric inputs

The surface cards have to be defined in the second block of the Monte Carlo input code. Every surface is defined by a surface number, a surface type and a corresponding surface card entry. In the manual all surface types and card entries can be found. The surfaces of the scintillation screen can be made in this way and may for example written as

```

11  px    0
12  px    1
13  py   -10
14  py    10
15  pz   -6
16  pz    6

```

For instance, the surface that corresponds to surface number 11 is defined as the plane that is perpendicular to the  $x$ -direction (px) and that intersects the  $x$ -axis at the origin (the surface card entry is 0). The surface that corresponds to surface number 15 is defined as the plane that is perpendicular to the  $z$ -direction (pz) and that intersects  $z = -6$  (the surface card entry is -6). The dimensions of all card entries are in centimeters. The defined surfaces are still infinitely large and thus do not yet describe a confined volume. This can be done with the cell cards.

The cell cards have to be defined in the first block of the MCNPX input code. Each cell can be defined using the cell number, the material number that is defined in the data card block and the corresponding density. The cell is defined by the surface numbers and form the boundary of the volume. The geometry of the scintillation screen can be written as

```

1  2  -7.34  11  -12  13  -14  15  -16

```

The cell corresponding to cell number 1 is made of material 2 and has a density of 7.34 g/cm<sup>3</sup>. If the density is written without the minus sign in front of it, it is defined in units of atoms/cm<sup>3</sup>. In



labelled as  $(0, 0, 0)$ . The order of the surface numbers in the lattice cell determine in which fashion the voxels are labelled, as can be seen in figure 6.  $(1, 0, 0)$  is the voxel that lies beyond the first surface number that is listed in the lattice cell. In the same way  $(-1, 0, 0)$  is the voxel that lies beyond the second surface that is listed in the lattice cell. All voxels in the screen can be labelled in this way.

### 3.2.3 Physical inputs

The data cards have to be defined in the third block of the MCNPX input code. The importance cards, tallies and material specifications have to be specified in the data cards and are discussed in this section. The MCNPX input code of this study has been extended from an earlier input code so that the source specification and the specification on the particles that are followed in the simulation have been copied entirely. Therefore, the latter specifications are not discussed.

Importance cards can for instance be useful if one wants to add a boundary to the problem region in order to save computational time. In this case, a void region that encloses the problem region can be defined in a cell card by replacing the material number by zero. There is no corresponding density that has to be written down. By assigning the `imp = 0` command to the corresponding cell, particles are no longer followed in that cell. This command can be written in a cell card or in a data card. If it is written in a data card, the importance of every cell card has to be written in the same order as the cell cards are defined. The importance can be defined for every particle that is followed in the simulation.

The information that has to be shown in the output file has to be defined in the code. The F tally card can be used for this. The simulation in this report uses two different F tally cards, namely the F2 and F6 card. The F2 tally needs a specified surface number and calculates the averaged flux of a surface. The F6 tally needs a specified cell number and calculates the averaged energy deposition of a cell. Both tallies can be combined with the lattice cards that have been mentioned before. In that case, the F2 and F6 tally commands may respectively look like

```
F2:h (21 < 2[0:0 0:19 0:29] < 1)
SD2 1 599r

+F6 (2 < 2[0:0 0:19 0:29] < 1)
SD6 7.34 599r
```

The first code means that the proton flux averaged over surface 21 is calculated for every voxel in the scintillation screen. This can be understood as follows. Cell number 1 corresponds to the cell that forms the complete scintillation screen. Cell number 2 is the origin voxel of the screen of which surface number 21 is the front surface. The number of voxels that fit in the scintillation screen have to be specified inside the square brackets. In this example the screen consists of one voxel in the  $x$ -direction, 20 voxels in the  $y$ -direction and 30 voxels in the  $z$ -direction. The F2:h command makes sure that only protons (h) are tallied and that other particles are not considered.

The second code means that the energy deposition averaged over cell 2 is calculated for all particles that are considered in the simulation. Note that the F6 tally is written in the same way, except that surface number 21 is replaced by cell number 2. This is because the F6 tally can only calculate the energy deposition in cells and not in surfaces. The +F6 command makes sure that all particles that are considered in the simulation are tallied.

Tally types F2 and F6 require a segment divisor (SD) card. This addition is required because MCNPX has trouble with calculating the exact areas and volumes of the surfaces and cells. For an F2 tally, the number that is specified in the SD card represents the area of the voxel in  $\text{cm}^2$ , which in the example is  $1 \text{ cm}^2$ . In the case of an F6 tally, the number represents the mass of the voxel in g, which in the example is 7.34 g. The area or mass that is written in the SD card should be specified for every voxel. In the example, the screen consists of 600 voxels so that 600 numbers should be specified. The code 599r makes sure to repeat the area or mass number 599 times. The output of the simulation yields the correct averaged flux or energy deposition in every voxel if the right areas and masses are used in the SD card, respectively.

The data that is obtained by the Monte Carlo simulation is used to reject the protons that have scattered significantly in the material. A so called cosine card is needed in order to distinguish between scattered and unscattered protons. The cosine card can be used in combination with the F2 tally on a certain surface to create different cosine bins. A cosine bin is a certain interval of scattering angles  $\theta_0$ . As in figure 3, every scattering angle is measured with respect to the initial direction of the proton which for the following example is taken to be 0 degrees and perpendicular to the surface. If a cosine bin runs for instance from 0 to 5 degrees, it contains all protons that have incident angles between -5 and 5 degrees. A cosine bin that runs from 5 to 180 degrees contains all protons that have incident angles between 5 and 180 degrees and that have incident angles between -5 and -180 degrees. The MCNPX code that distinguishes between the different scattering angles reads

```
F2:h (21 < 2[0:0 0:19 0:29] < 1)
SD2 1 599r
*C2 5 0
```

where the first two lines are identical to the F2 tally before. The asterisk in front of C2 indicates that the numbers should be given in units of degrees. From now on, the angle that specifies the cosine bin is called the binning angle and in the example is 5 degrees. Two cosine bins are defined in such a way that cosine bin 1 runs from 5 to 180 degrees and cosine bin 2 runs from 0 to 5 degrees. The data that is obtained by cosine bin 1 is used to represent all protons that have scattered. In the same way, cosine bin 2 represents all protons that have not scattered. The Monte Carlo code should be written without mentioning the 180 degrees, because this is already implied by the code. The output of the code shows two data sets of the proton flux. The first data set corresponds to the first bin and the second data set corresponds to the second bin.

The last physical input to be discussed is the material specification. As discussed before, a material number has to be specified in every cell card except if the cell card describes a void region. All materials are specified in the data block. The general material specification looks like

```
Mi ZZZAAA1 fraction1 ZZZAAA2 fraction2 ...
```

where  $i$  is an arbitrary material number. Every element can be specified by a ZZZAAA and fraction where ZZZ is the atomic number and AAA the atomic mass number. If AAA = 0, the naturally occurring element is meant. The fractions are normalized by MCNPX. Using this notation, material 2 may for example look like

```
M2 16032 1 8016 2 64000 2
```

Material number 2 consists of sulfur-32, oxygen-16 and the naturally occurring isotopes of gadolinium with an isotopic abundance of 20%, 40% and 40%, respectively. Cell 3 from the example has a material number of 2 and thus refers to this material specification in the data block. Hence, cell 3 is a filling universe that consists of sulfur, oxygen and gadolinium. Note that the density of the material is not specified in the data card, but only written in the cell card.

### 3.3 Setup of the Monte Carlo simulation

In this section the geometry mimicking the experimental setup that has been used in the Monte Carlo simulation is discussed in more detail and shown in figure 7. The dimensions of every component are not specified in this section but can be looked up in the complete input file that is given in appendix A. Every number in figure 7 refers to the corresponding cell card in the code and the distance of a component from the proton source is given in the figure. From now on, the surface that is the closest to the proton source is called the upstream surface. The surface that is the furthest from the proton source is called the downstream surface.

The problem region (998) is enclosed by a void (999) that has an importance of zero. The problem region is filled with air. The proton beam is travelling in the  $+x$ -direction (from left to right) and starts just in front of the aramica exit foil (10). After traversing the foil, the protons travel through the first collimator (20) and are scattered by the scatter foil (30). The scatter foil

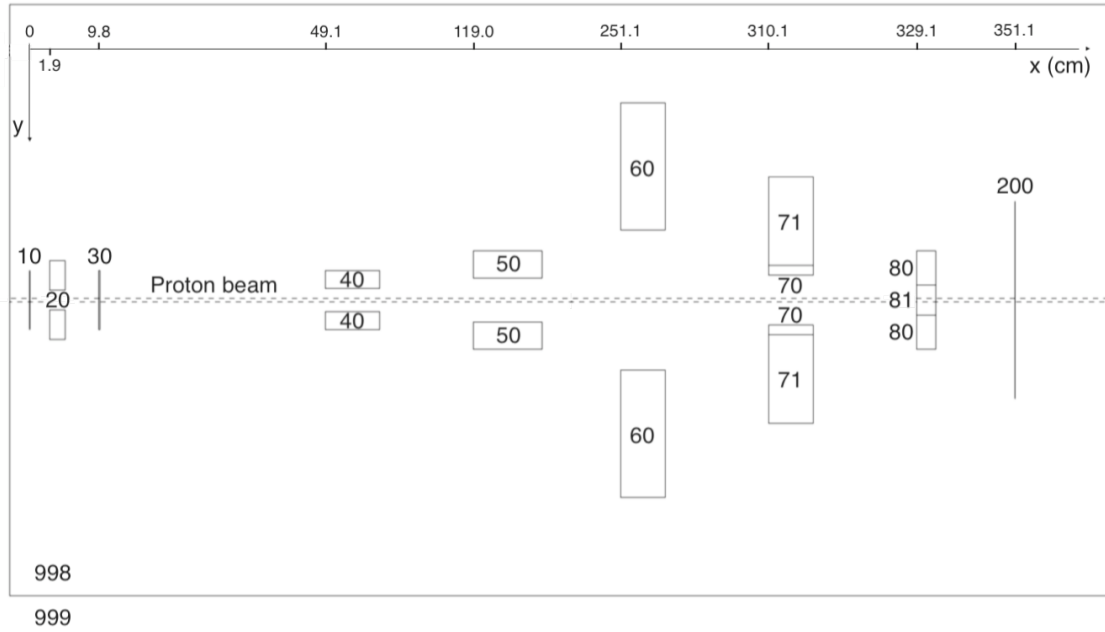


Figure 7: The setup of the experiment and corresponding Monte Carlo simulation. All components are numbered by their cell number that corresponds to the Monte Carlo input file in appendix A. The distance from each component to the proton source is specified, however the figure is not drawn to scale.

is made of lead and causes the proton width to increase. Collimators are used to limit the width of the proton beam. They are placed at such distance from the scatter foil that the proton beam is sufficiently parallel to the initial proton direction and that the proton flux entering the body is sufficiently high. Collimators 2, 3 and 4 have cell number 40, 50 and 60, respectively. The geometry of collimator 5 has been made differently with respect to the other collimators and is therefore discussed in more detail.

As is shown in figure 7, the fifth collimator consists of cell number 70 and 71 which are an inner hollow cylinder and outer cylinder, respectively. The only difference between both cells is the importance that has been assigned to them. Cell 71 and all other collimators have an importance of zero for all particles, whilst cell 70 has an importance of 1 for all particles. This has been done for the following reason. The probability that a proton enters a collimator, leaves the collimator and ends up at the scintillation screen (200) is considered to be negligible. If a particle travels through a collimator that has an importance of zero, MCNPX stops following the particle from the moment that the particle is entering that collimator. This means that all particles that enter a collimator of zero importance will be gone and therefore are not able to arrive at the scintillation screen. This saves computational time. However, the probability that a proton enters cell 70 of the collimator, leaves cell 70 and ends up at the scintillation screen is of larger probability because cell 70 belongs to the collimator that is the closest to the screen. Therefore, an importance of 1 has been labelled to cell 70.

After passing the last collimator, the protons enter the phantom. The phantom represents a highly simplified tissue that is divided into an inner (81) and outer cylinder (80). As is shown in figure 8, these cylinders are made of cortical bone and solid water, respectively. The density of solid water ( $1.045 \text{ g/cm}^3$ ) is comparable to that of water. Cortical bone has a much higher density ( $1.823 \text{ g/cm}^3$ ) and mimics human bone.

After the protons have travelled through the phantom they enter the scintillation screen (200). The scintillation screen has been entirely filled up with voxels (201, not in the figure). Every voxel is made of a filling universe (900, not in the figure) that is made of gadolinium oxysulfide (material 1 in appendix A). In this way, every voxel and thus the entire scintillation screen consists of material

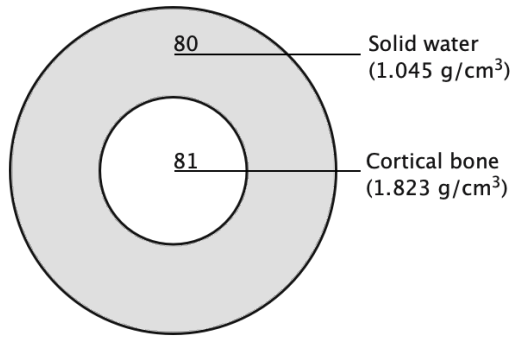


Figure 8: A cross section of the phantom that has been used in the experiment and simulation. The outer cylinder (80) consists of solid water and the inner cylinder (81) consists of cortical bone.

1. The structure of the code that has been used to describe the scintillation screen is the same as in the example with cell 1, 2 and 3 that has been explained before. The orientation of the screen has been chosen so that the upstream and downstream surfaces of the screen are perpendicular to the  $x$ -direction. The surface numbers of the voxels are defined in such a way that the origin voxel  $(0,0,0)$  corresponds to the voxel in the bottom left corner of the scintillation screen, as is shown in figure 9. Some more voxel labels are shown as an example. The order of the surface numbers in lattice cell 201 are defined so that the second and third indices of the voxel label are increasing by one step for every next voxel in the  $y$ - and  $z$ -direction, respectively. The first index of the voxel label is always zero, because the thickness of the scintillation screen is one voxel.

In order to make sure that the Monte Carlo simulations can be compared with the experiment, the voxel size is chosen to be identical to the pixel size of the CCD camera. The CCD camera contains of 768 by 512 pixels and 43 pixels fit exactly in 1 cm of the camera in both the  $y$ - and  $z$ -direction. The thickness of the scintillation screen is chosen so that it is identical to the pixel width. This means that every voxel in the screen is a cube of which all sides are approximately equal to  $233 \mu\text{m}$ . The length of each side of the scintillation screen is defined to be the pixel size times the number of pixels along that side. In this way, the dimensions of the  $y$ - and  $z$ -direction of the scintillation screen are determined to be 17.86 cm and 11.91 cm and contain 768 and 512 voxels, respectively.

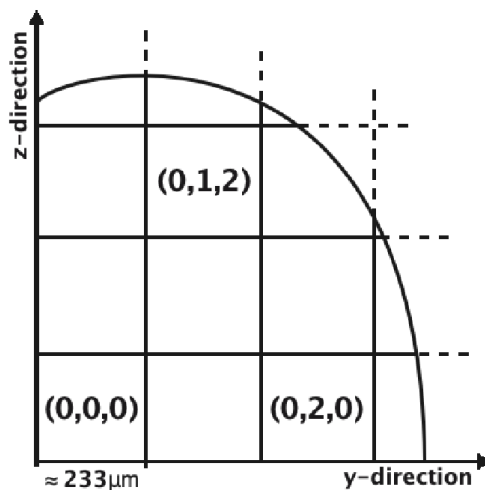


Figure 9: The bottom left corner of the scintillation screen to illustrate the voxel numbering in the MCNPX input file. The screen consists of cubic voxels with all sides approximately equal to  $233 \mu\text{m}$ .

### 3.4 Combining the F2 and F6 tally

An F6 tally is used on cell 201 (voxel) to obtain the averaged energy deposition in every voxel. A cosine card in combination with an F2 tally is used on surface 860 to reject all scattered protons, i.e. the protons that enter the scintillation screen with an angle larger than the binning angle. For some simulations no cosine cards have been used. The code that is needed for the F cards has been written in the same way as the F tally code described previously and can be looked up in appendix A.

The purpose of the Monte Carlo simulation is to correct the radiograph that has been obtained by the experiment for multiple Coulomb scattering. This radiograph does not have a constant flux in front of the scintillation screen, because some protons have scattered by the phantom. Therefore, the results that have been obtained by the CCD camera in the experiment are not normalized for the proton flux and should therefore be corrected. This correction has been done by dividing the data values per voxel by the unscattered proton flux of that same voxel. In this way, the protons that have scattered are indirectly rejected from the radiograph. The correction has been done for different binning angles to investigate the influence of the binning angle on the quality of the corrected radiograph.

## 4 Results

As mentioned previously, the Monte Carlo simulations have been done in order to simulate the energy deposition of protons on the scintillation screen. A phantom is placed in between the proton source and the screen to investigate how the sharpness of the radiograph is affected by multiple Coulomb scattering. The F2 tally in combination with a cosine card has been used to reject the scattered protons from the radiograph that has been obtained by the experiment. Simulations have been done for different binning angles and all simulations have run for 3000 minutes. The data from all simulations and experiments have been converted to radiographs by MATLAB [28]. The MATLAB codes that have been used to convert the F2 and F6 tally to the corresponding radiograph can be looked up in appendix B and C, respectively. A median filter has been used to remove noise from the data.

### 4.1 Radiographs of the averaged proton energy deposition

The radiograph that has been obtained from the simulation without the phantom is shown in figure 10a. Except for the phantom, all other components that are shown in the setup have been used in this simulation and are placed at the distances that are specified in figure 7. The energy deposition is higher for voxels that are darker and it can be seen that the energy deposition of the protons in the center of radiograph is approximately the same. To make this more clear, in figure 10b

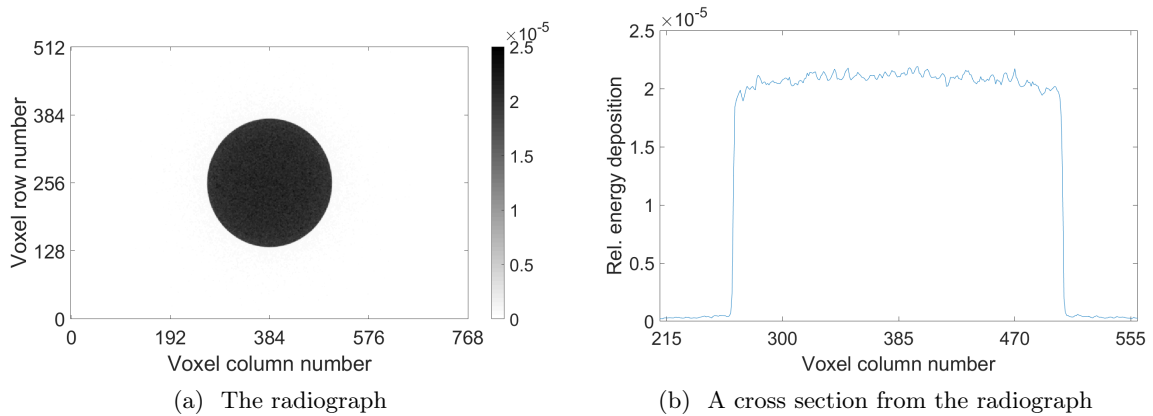


Figure 10: The radiograph (a) of the simulated relative energy deposition of protons in the scintillation screen without the phantom. A cross section (b) of the radiograph is made and obtained by averaging voxel row numbers 251 to 260.

a cross section is shown of the relative energy deposition versus the voxel column numbers. The relative energy deposition is averaged over voxel row numbers 251 to 260. It can be seen that the energy deposition of the voxels in the center of the radiograph is indeed approximately constant. The energy deposition decreases abruptly to zero around voxel column numbers 265 and 505. This means that the diameter of the region of high energy deposition is approximately 5.6 cm, which roughly corresponds to the diameter of the fifth collimator of 5 cm. The radius of the proton beam becomes thus slightly larger if it travels further along the  $x$ -direction. The fifth collimator is placed at such distance from the scatter foil that the proton beam can be considered to enter the phantom perpendicularly to its front surface. The increase in the width of the proton beam can be explained by the proton scattering inside the phantom.

The radiograph in figure 11a is obtained by placing the phantom in between the source and the screen. The shape of the phantom can be recognized in the inner and outer region of the radiograph, which are respectively assigned to be region A and B. However, the transition between region A and B in the radiograph is not as sudden as in reality. In fact, the energy deposition of the outer region has increased and the energy deposition of the region (C) in between the inner and outer region has decreased with approximately the same amount, as can be seen in figure 11b. Also note that the energy deposition in region A is lower than in region B. The particular shape of the energy deposition in figure 11b can be interpreted as follows. The protons that travel through region C have scattered by the cortical bone so that they mainly enter the screen in region B. The majority of the scattered protons thus ends up in the outer region whilst a small part ends

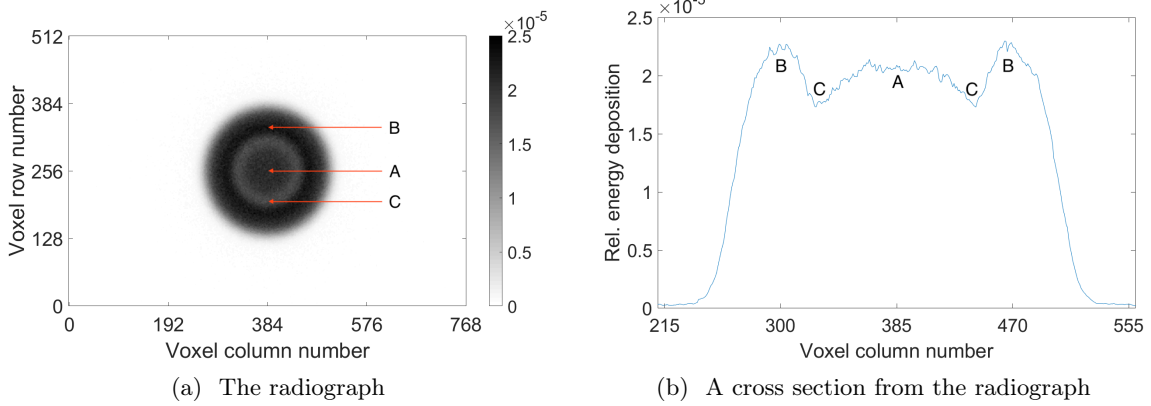


Figure 11: The radiograph (a) of the simulated relative energy deposition of protons in the scintillation screen. A cross section (b) of the radiograph is made and obtained by averaging voxel row numbers 251 to 260.

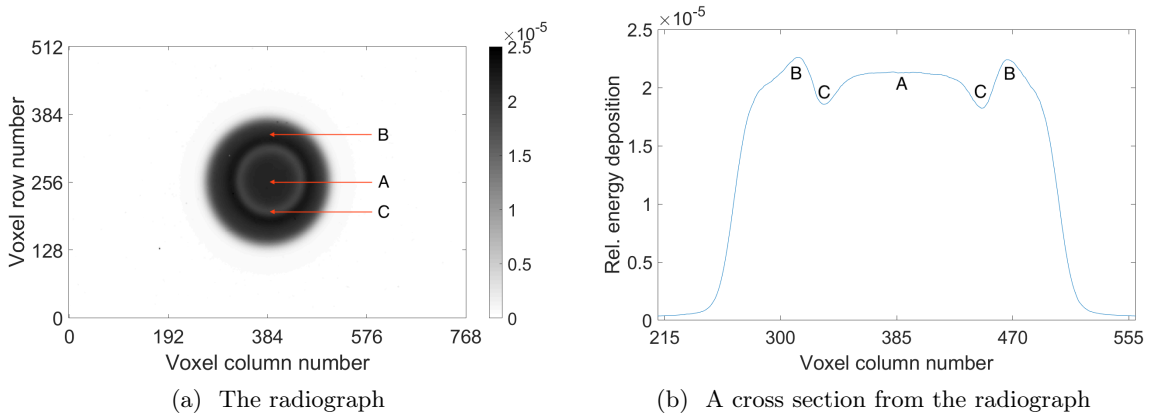


Figure 12: The radiograph (a) of the relative energy deposition of protons in the scintillation screen obtained experimentally. A cross section (b) of the radiograph is made and obtained by averaging voxel row numbers 251 to 260.

up in the inner region. For this reason, the transition boundary of the inner to the outer region that is shown in the radiograph is not very sharp. The edges of region B in figure 11 are less sharp compared to figure 10 because the slope of the relative energy deposition as function of voxel column number is less steep, as can be seen in figure 11b. Because of the fact that the transition between region A and B is not sudden and that the edges of region B are not sharp, the prediction of the proton stopping powers by the planning CT can not be improved by this radiograph.

The radiograph that has been obtained experimentally at KVI-CART is shown in figure 12a. By comparing it to the radiograph of figure 11a, it can be seen that the shape of both is very similar. From figure 12b it can be seen that the majority of the protons have also scattered from region C to B. As in figure 11b, a small part of the protons has scattered towards region A. Hence, the simulated radiograph from figure 11 matches the radiograph that is obtained experimentally very well. However, the inner region of the radiograph that is shown in figure 12a seems to be slightly off center so that the radiograph is slightly asymmetric.

## 4.2 Radiographs of the averaged proton flux

In order to reject the scattered protons from the data that is obtained by the F2 tally in the simulations, cosine cards are used. In order for the cosine card to distinguish between protons that have scattered and protons that have not scattered, the binning angle has to be specified. As explained before, the binning angle determines the interval of the cosine bins, so that more protons are rejected if the binning angle is small. Monte Carlo simulations have been done for binning angles of 0.5, 0.75, 1, 1.5 and 2 degrees. The radiographs corresponding to these angles are shown in figure 13, 14, 15, 16 and 17, respectively. The values per voxel that are obtained by the F2 tally are divided by the sum of all the voxels in order to normalize the radiographs. For all figures, the contrast between the inner and outer region of the radiograph is important because this determines to which extent the regions can be distinguished.

In figure 13a a radiograph is shown of the simulated relative proton flux that enters the screen where all protons with an angle belonging to bin 1 have been rejected from the data set. For a binning angle of 0.5 degrees, this means that all protons that enter the screen with an angle between -0.5 and 0.5 degrees are included in the data set and that protons that enter the screen with different angles are rejected from the data set. In figure 13b it can be seen that the averaged proton flux that enters the screen in region A is smaller compared to region B (and note that there is no region C). However, the averaged proton flux is equally distributed before the protons travel through the phantom. This means that most protons have been scattered by the inner cylinder of the phantom. By rejecting the scattered protons from the data, the transition from region A to B becomes very sharp, as can be seen in figure 13.

By comparing figure 13 to figure 14, 15, 16 and 17, it can be seen that the contrast between

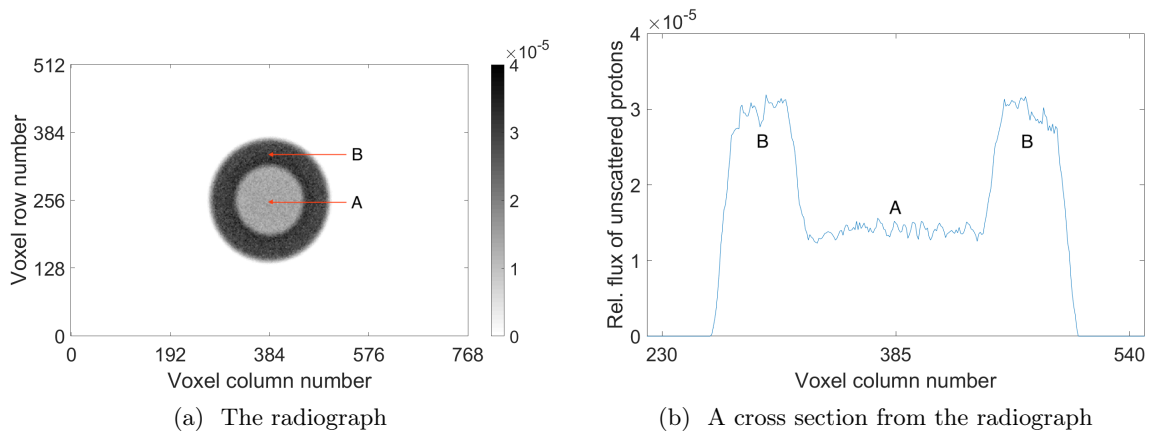


Figure 13: The radiograph (a) of the simulated relative flux of unscattered protons entering the scintillation screen for a binning angle of 0.5 degrees. A cross section (b) of the radiograph is made and obtained by averaging voxel row numbers 251 to 260.

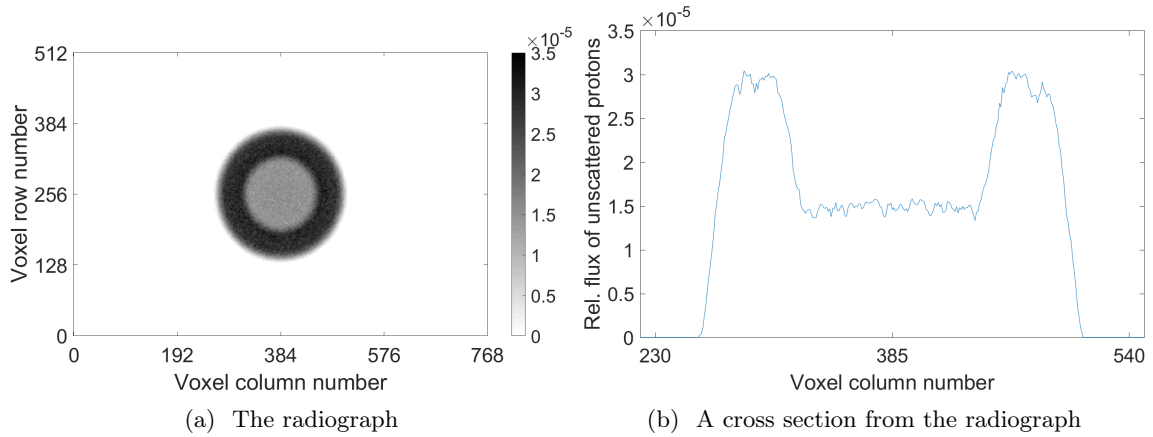


Figure 14: The radiograph (a) of the simulated relative flux of unscattered protons entering the scintillation screen for a binning angle of 0.75 degrees. A cross section (b) of the radiograph is made and obtained by averaging voxel row numbers 251 to 260.

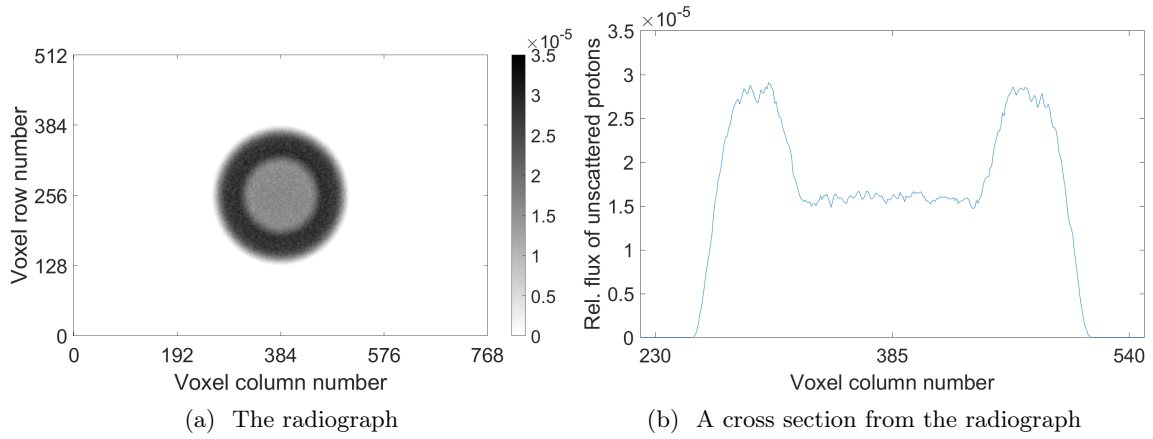


Figure 15: The radiograph (a) of the simulated relative flux of unscattered protons entering the scintillation screen for a binning angle of 1 degrees. A cross section (b) of the radiograph is made and obtained by averaging voxel row numbers 251 to 260.

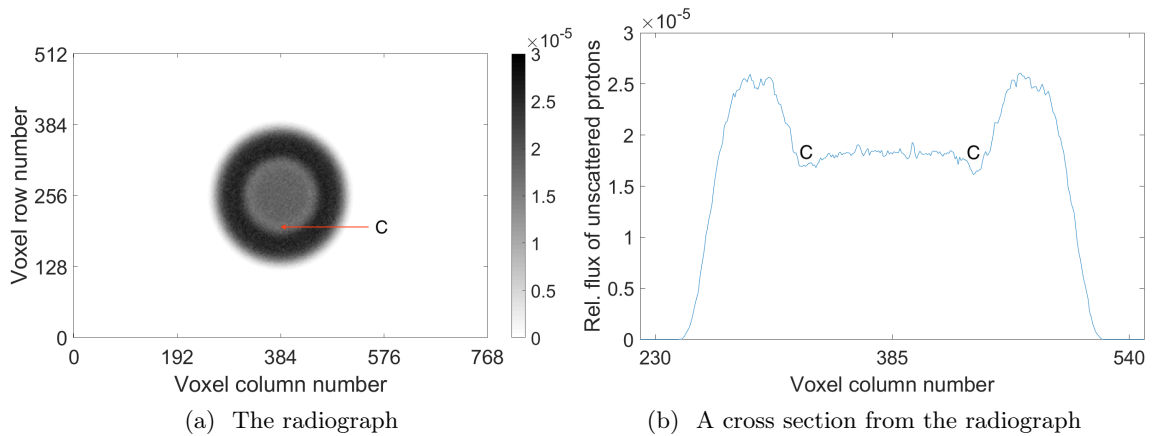


Figure 16: The radiograph (a) of the simulated relative flux of unscattered protons entering the scintillation screen for a binning angle of 1.5 degrees. A cross section (b) of the radiograph is made and obtained by averaging voxel row numbers 251 to 260.

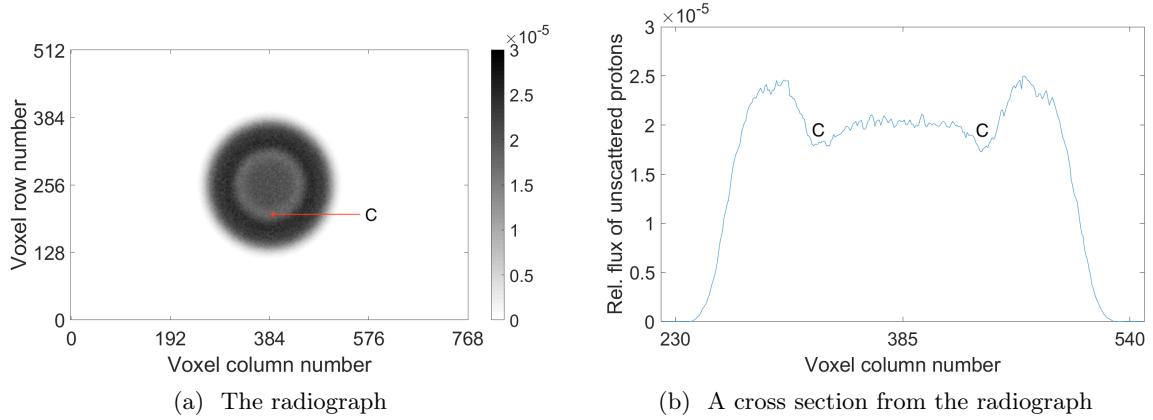


Figure 17: The radiograph (a) of the simulated relative flux of unscattered protons entering the scintillation screen for a binning angle of 2 degrees. A cross section (b) of the radiograph is made and obtained by averaging voxel row numbers 251 to 260.

the inner and outer region is decreasing for larger binning angles. To express the contrast in a quantitative way, the relative proton flux in region B has been divided by the relative proton flux in region A. For every region, the flux is averaged over a certain number of voxel column numbers, depending on the width of the region. A graph of the fraction versus the binning angle is shown in figure 18. A large fraction gives rise to a large contrast between the regions and is obtained for small binning angles. However, the quality of the radiograph does not only depend on the contrast between the inner and outer region. Also, the relative error of the data is significant for the accuracy of the radiograph. The relative error in the data is determined by MCNPX for every obtained value in the F2 and F6 tally. Using the obtained errors, the relative error of the averaged proton flux in the inner region of the radiograph is determined to increase for smaller binning angles, as can be seen in figure 19. It is approximately 0.242 for a binning angle of 0.5 degrees and decreases to 0.086 for a binning angle of 2 degrees. This is because the number of unscattered protons that enter the screen become less. In order to obtain a radiograph that can eventually be used to accurately convert the energy deposition to the proton stopping power, a compromise has to be made between the fraction from figure 18 and the relative error from figure 19.

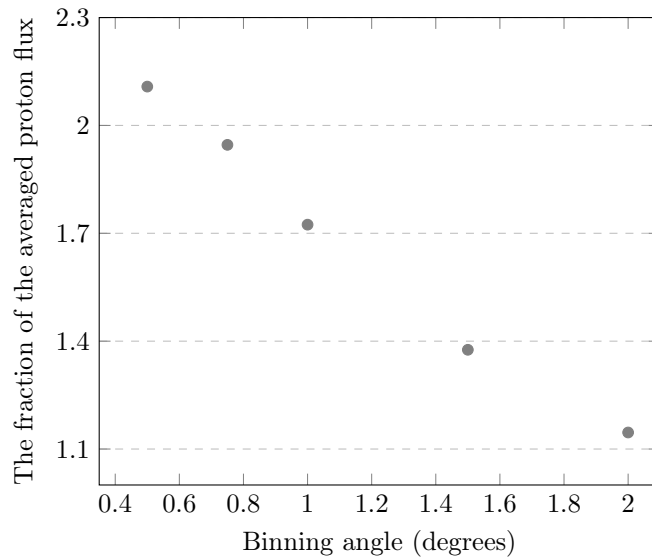


Figure 18: The fraction of the averaged proton flux between the outer and inner region of the radiograph versus the binning angle

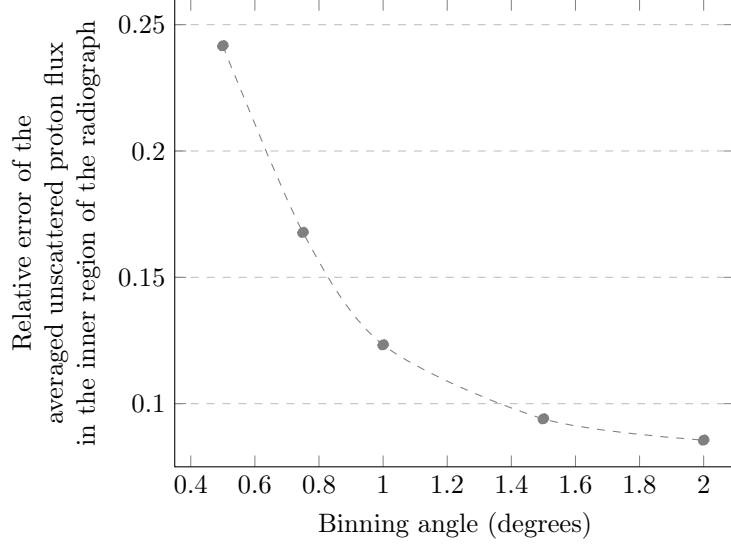


Figure 19: The relative error of the averaged unscattered proton flux in the inner region of the radiograph versus the binning angle for a simulation time of 3000 minutes

As discussed before, in figure 11 a region (C) of lower energy deposition can be seen in between region A and B of the radiograph. This region becomes again visible in figure 16 and 17 in which binning angles of 1.5 and 2 degrees are used, respectively. For larger binning angles, less proton are rejected from the radiograph. Therefore, the radiographs in figure 16 and 17 do not have a sharp transition between region A and B. These radiographs can thus not be used to accurately convert their data to proton stopping powers.

### 4.3 Corrected radiographs of the averaged proton energy deposition

As explained before, the radiograph obtained by the experiment that is shown in figure 12 can be corrected for multiple Coulomb scattering by dividing the data values per voxel by the unscattered proton flux of that same voxel. By doing this, the radiograph from figure 12 is also normalized for the number of protons that enter the scintillation screen. Figure 16 and 17 are not used for the correction, because the transition between the inner and outer region of the radiographs was

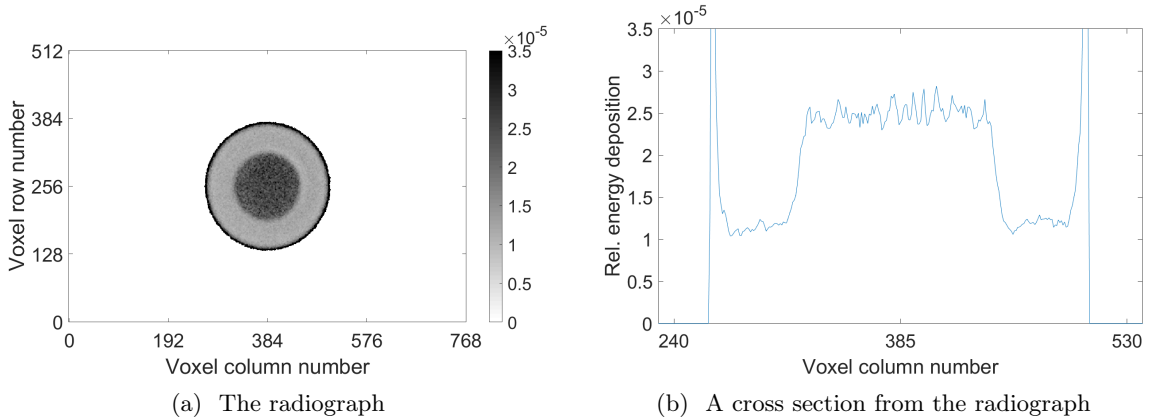


Figure 20: The radiograph (a) of the relative energy deposition of protons in the scintillation screen obtained experimentally, that is corrected for multiple Coulomb scattering using a binning angle of 0.5 degrees. A cross section (b) of the radiograph is made and obtained by averaging voxel row numbers 251 to 260.

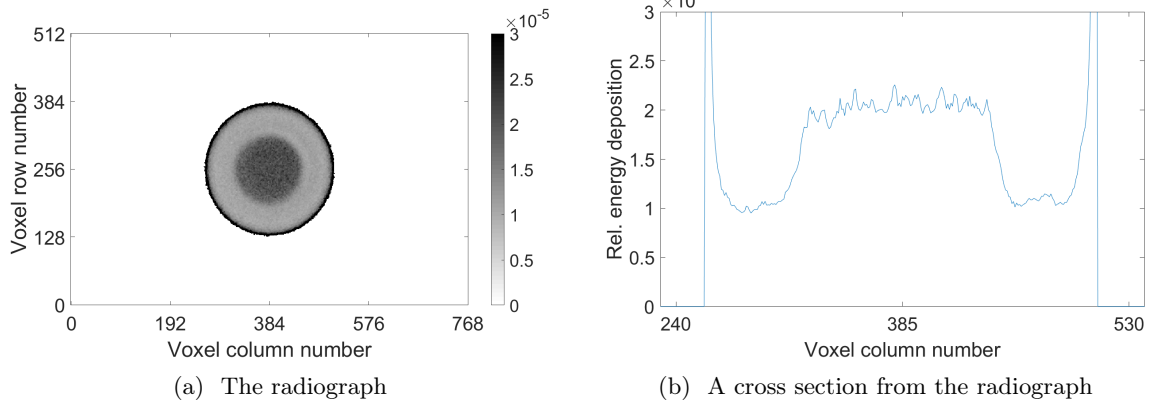


Figure 21: The radiograph (a) of the relative energy deposition of protons in the scintillation screen obtained experimentally, that is corrected for multiple Coulomb scattering using a binning angle of 0.75 degrees. A cross section (b) of the radiograph is made and obtained by averaging voxel row numbers 251 to 260.

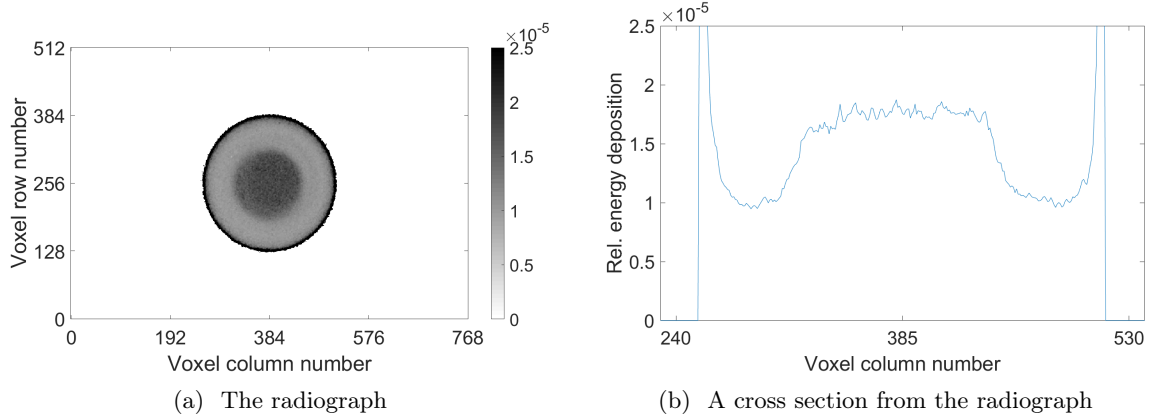


Figure 22: The radiograph (a) of the relative energy deposition of protons in the scintillation screen obtained experimentally, that is corrected for multiple Coulomb scattering using a binning angle of 1 degrees. A cross section (b) of the radiograph is made and obtained by averaging voxel row numbers 251 to 260.

shown to be not very sharp.

In figure 20, the corrected radiograph of the energy deposition of the protons is shown together with the corresponding cross section. The range of the values of the relative energy deposition in figure 20 is chosen so that the contrast between the inner and outer cylinder is clearly visible. For the cross section in figure 20b, this means that the values of the relative energy deposition have been cut off at a certain value. However, this is not a problem because the contrast between the inner and outer region is the point of interest. Protons that have scattered have been rejected from the data using a binning angle of 0.5 degrees. Figure 20 is obtained by dividing every voxel of the radiograph of figure 12 by the flux of unscattered protons corresponding to that same voxel from figure 13. Because of this division, the energy deposition in the inner region of the radiograph of figure 20 is higher than in the outer region. The image of figure 20a is enclosed by a thin circle of high energy deposition, because the unscattered proton flux is very low at the far edge of the outer region, as can be seen in figure 13. The region (C) of low energy deposition that can be seen in figure 12 can also be recognized in figure 20, however to a lesser extent.

Figures 21 and 22 show the radiographs that are obtained after correcting figure 12 by figure 14 and 15, respectively. From figure 21b it can be seen that the transition from the inner to the outer region is almost as sudden as in figure 20b and thus both regions can be distinguished very well. However, the contrast between the regions gets slightly lower if a binning angle of 0.75 degrees is

used gets even lower for a binning angle of 1 degrees. Also, the transition from the inner to the outer region becomes less sharp. As discussed previously, the radiograph in figure 12 is slightly asymmetric. Note that this asymmetry becomes more visible if larger binning angles are used.

## 5 Discussion

In this section the accuracy of the results is reviewed and some results are checked by calculations. Also, several points of improvement are discussed.

### 5.1 Accuracy of the radiographs

In this report different Monte Carlo simulations have been done. Figure 11a shows the radiograph that has been obtained by simulating the setup from figure 7. This radiograph is shown to be very similar to the radiograph that has been obtained by experiment. The relative error of the data of voxel row numbers 251 to 260 in figure 11 is averaged for every voxel column number and is shown in figure 23. The relative error is approximately 0.07 in the center of the radiograph and increases rapidly to higher values at the edges of the radiograph. By comparing figure 23 to figure 11b, it can be seen that the energy deposition becomes inaccurate for voxels that have a proton energy deposition of approximately zero. However, the accuracy is much higher for voxels that have a nonzero proton energy deposition. In this report, only the accuracy in the center of the radiograph is of importance, so it is not a major problem that the energy deposition becomes uncertain at the edges of the radiograph.

### 5.2 Comparison with literature

Figure 12 has been corrected for multiple Coulomb scattering of which the results were shown in figure 20, 21 and 22. The ratio of the energy deposition between the inner and outer region has been determined for each binning angle from these figures. Before calculating the ratio between the regions, the energy deposition in every region is averaged over a certain number of voxel column numbers, depending on the width of the region. In this way, the ratios are determined to be 2.005, 1.817 and 1.487 corresponding to binning angles of 0.5, 0.75 and 1 degrees, respectively.

In order to compare the obtained ratios, a calculation has been done using data provided by SRIM [29]. No error analysis has been done because this calculation only serves as a rough check of the literature. A 190 MeV proton that travels straight through cortical bone (the inner region of the phantom) has a stopping power of 0.7648 MeV/mm. The phantom has a thickness of 19.6 mm.

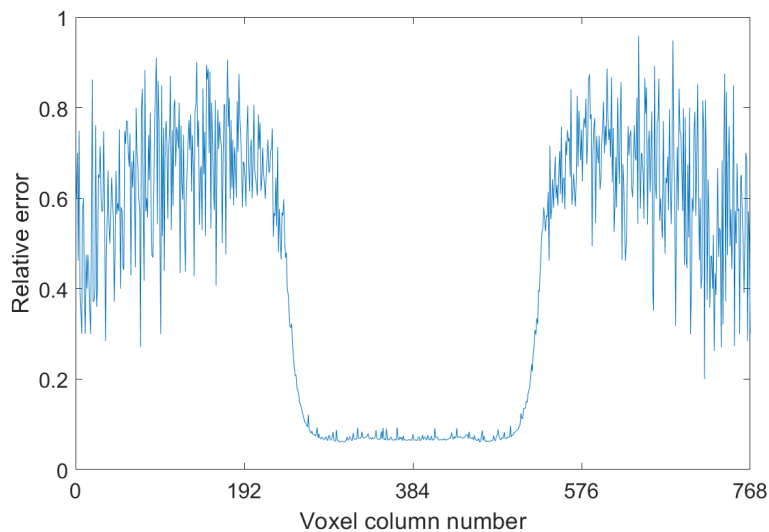


Figure 23: The relative error of the simulated energy deposition of protons in the scintillation screen, averaged over voxel row numbers 251 to 260.

Therefore, the proton energy after leaving the cortical bone is determined to be approximately 175 MeV. A 190 MeV proton that travels straight through solid water (the outer region of the phantom) has a stopping power of 0.4786 MeV/mm and thus the proton energy after leaving the solid water is determined to be approximately 180 MeV. In this calculation it is assumed that the proton stopping power remains constant while the proton traverses the phantom. This assumption is valid because after passing through the phantom, the proton stopping power in solid water and cortical bone increases only by 3.5 and 4.6 percent from the initial stopping power, respectively. The proton stopping power in the scintillation screen (that consists of gadolinium oxysulfide) that corresponds to the 175 MeV and 180 MeV proton is determined to be 2.136 MeV/mm and 2.099 MeV/mm, respectively. By dividing these stopping powers, the ratio of the energy deposition between the inner and outer region of the phantom is determined to be 1.018.

The ratios obtained from the simulations do not agree with the calculations. In fact, the ratios differ between a factor 1.4 and 2, depending on the binning angle. Moreover, the calculated ratio does not depend on the binning angle. However, by comparing figure 20, 21 and 22, it can be seen that the ratio between the energy deposition in both regions should certainly depend on the binning angle. The difference in the ratios may have to do with the conversion from figure 12 to figure 20, 21 and 22. Further research may look into this dissimilarity.

### 5.3 Optimal binning angle and further research

The radiographs corresponding to binning angles of 0.5, 0.75 and 1 degrees have led to good quality images. However, a compromise has to be made in order to determine the optimal binning angle. The calculation of the ratio of the energy deposition between the inner and outer region of the radiograph has shown that the sharpness of the transition between the regions increases for lower binning angles. However, the accuracy of the averaged proton flux in the inner region of the radiograph decreases for lower binning angles, as was shown in figure 19. The radiograph corresponding to a binning angle of 0.75 degrees has a good amount of contrast between the inner and outer region and consists of data with a relative error of 0.17. The radiograph corresponding to a binning angle of 0.5 degrees has a slightly better contrast, however the relative error in the data is almost 1.5 times larger. The radiograph corresponding to a binning angle of 1 degree has a smaller contrast, however the relative error in the data has improved to 0.09. In this simulation, the radiograph that corresponds to a binning angle of 0.75 degrees is favoured over the other radiographs, because it has a good contrast and an error that is sufficient for the purpose of this report.

Further research may obtain lower relative errors by extending the simulation time. However, because of the inverse square root dependence between the relative error and the simulation time, the relative error decreases very slowly if the simulation time is increased. For instance, for the relative error to become twice as small, the simulation time has to be increased by a factor 4. Relative errors may also be reduced by using a Monte Carlo code that is more efficient. The process to determine the optimal binning angle can be investigated more extensively in order to obtain a radiograph that has higher contrast and accuracy. Keeping in mind that the final purpose is to improve the accuracy of proton radiography of human tissues, a more advanced phantom can be used. For instance, a phantom that consists of materials that do not lie parallel to the beam direction can be used as a next step.

## 6 Conclusion

In this report, a first step has been made in improving treatment planning by proton radiography in order to improve the accuracy of proton therapy. For this purpose, Monte Carlo simulations have been done to study the effect of the rejection of scattered protons on the quality of the radiograph. Protons have traversed through a highly simplified tissue which was placed in front of the scintillation screen. The geometry of the simulations were identical to the setup of an experiment that has been previously done at KVI-CART.

The radiograph of the energy deposition that was obtained by the Monte Carlo simulation and that was obtained experimentally show significant similarities in shape and relative energy deposition. Multiple radiographs of the averaged proton flux have been simulated in which the

binning angle was defined differently for every simulation. The radiographs corresponding to binning angles of 1.5 and 2 degrees do not have evident regions of constant proton flux and are not separated by a sharp transition. These radiographs can thus not be used to improve cancer treatment planning.

However, the radiographs corresponding to binning angles of 0.5, 0.75 and 1 degrees show sharp transitions between the regions of constant proton flux and were thus used to correct the radiograph that has been obtained experimentally. The optimal binning angle was determined by considering the relative error of the data and the contrast between the inner and outer region of the radiograph. The relative contrast between the regions was compared with a calculation and was determined to differ significantly with the simulated results. For the specific setup in this report, the radiograph corresponding to a binning angle of 0.75 degrees was determined to have the best quality. Further research may improve on the accuracy of the radiograph by studying the determination of the optimal binning angle more extensively. Moreover, a more efficient Monte Carlo code can be used to obtain lower uncertainties in the data. Also, more complex phantoms may be used to mimic the human tissue in a more realistic way.

## References

- [1] G. Poludniowski, N. Allinson, and P. Evans, “Proton radiography and tomography with application to proton therapy,” *Br J Radiol*, vol. 88, no. 1053, June 2015.
- [2] V. Bashkirov, R. Johnson, H. Sadrozinski, and R. Schulte, “Development of proton computed tomography detectors for applications in hadron therapy,” *Nuclear Instruments and Methods in Physics Research A*, vol. 806, pp. 120–129, 2016.
- [3] A. Knopf and A. Lomax, “In vivo proton range verification: a review,” *Phys. Med. Biol.*, vol. 58, pp. R131–R160, 2013.
- [4] R. Zhang, J. Fontenot, D. Mirkovic, J. Hendricks, and W. Newhauser, “Advantages of MCNPX-based lattice tally over mesh tally in high-speed Monte Carlo dose reconstruction for proton radiotherapy,” *Nuclear Technology*, vol. 183, pp. 101–106, 2013.
- [5] F. Olivari, Personal Communication, PhD student at KVI-CART, 2019.
- [6] E. Fokas, G. Kraft, H. An, and R. Engenhart-Cabillic, “Ion beam radiobiology and cancer: Time to update ourselves,” *Biochimica et Biophysica Acta (BBA) - Reviews on Cancer*, vol. 1796, no. 2, pp. 216–229, December 2009.
- [7] M. Berger, J. Coursey, M. Zucker, and J. Chang. ESTAR, PSTAR, and ASTAR: Computer Programs for Calculating Stopping-Power and Range Tables for Electrons, Protons, and Helium Ions (version 2.0.1). [Online]. Available: <http://physics.nist.gov/Star>
- [8] D. Grimes, D. Warren, and M. Partridge, “An approximate analytical solution of the Bethe equation for charged particles in the radiotherapeutic energy range,” *Scientific Reports*, vol. 7, no. 9781, 2017.
- [9] C. Leroy and P. Rancoita, “Heavy Ions,” in *Principles of radiation interaction in matter and detection*, 3rd ed. New Jersey: World Scientific Publishing Co. Pte. Ltd., 2012, ch. 2.1.4.1, pp. 93–99.
- [10] H. Paul, “Nuclear Stopping Power And Its Impact On The Determination Of Electronic Stopping Power,” *AIP Conf. Proc.*, vol. 1525, pp. 309–313, 2013.
- [11] W. Newhauser and R. Zhang, “The physics of proton therapy,” *Physics in Medicine and Biology*, vol. 60, 2015.
- [12] L. Cerrito, “Multiple Scattering,” in *Radiation and Detectors: Introduction to the Physics of Radiation and Detection Devices*. London: Springer International Publishing AG, 2017, ch. 6.4, pp. 104–106.

- [13] K. Nakamura *et al.*, “Review of particle physics,” *JP G*, vol. 37, 2012, chapter 27.3.
- [14] W. Cottingham and D. Greenwood, “The passage of energetic particles through matter,” in *An Introduction to Nuclear Physics*, 2nd ed. Bristol: Cambridge University Press, 2001, ch. 14, pp. 199–213.
- [15] B. Gottschalk, A. Koehler, R. Schneider, J. Sisterson, and M. Wagner, “Multiple Coulomb scattering of 160 MeV protons,” *Nuclear Instruments and Methods in Physics Research Section B: Beam Interactions with Materials and Atoms*, vol. 74, no. 4, pp. 467–490, 1993.
- [16] D. Williams, “The most likely path of an energetic charged particle through a uniform medium,” *Physics of Medicine and Biology*, vol. 49, no. 13, 2004.
- [17] S. Meroli. Multiple scattering for particles in matter. [Online]. Available: [http://meroli.web.cern.ch/lecture\\_multiple\\_scattering.html](http://meroli.web.cern.ch/lecture_multiple_scattering.html)
- [18] E. van der Graaf, “Advanced X-ray CT and proton imaging for proton therapy,” 2017.
- [19] The Bragg Peak: The Foundation of Proton Therapy. [Online]. Available: <https://www.protominternational.com/2018/06/bragg-peak/>
- [20] H. Liu and J. Chang, “Proton therapy in clinical practice,” *Chin J Cancer*, vol. 30, no. 5, pp. 315–326, May 2011.
- [21] S. Jia *et al.*, “Designing a range modulator wheel to spread-out the Bragg peak for a passive proton therapy facility,” *Nuclear Instruments and Methods in Physics Research Section A: Accelerators, Spectrometers, Detectors and Associated Equipment*, vol. 806, pp. 101–108, January 2016.
- [22] M. Yagi, “Irradiation and Facility,” in *Elemental Analysis by Particle Accelerators*. CRC Press, 1992, ch. 10.IV.B.2, p. 434.
- [23] D. Pelowitz, *MCNPX USER’S MANUAL*, 2nd ed., April 2005.
- [24] M. James *et al.*, “MCNPX 2.7.X – New Features Being Developed,” October 2009.
- [25] T. Warnock, “Random-Number Generators,” *Los Alamos Science*, vol. 15, no. 1987, pp. 137–141.
- [26] E. Cashwell and C. Everett, *A Practical Manual on the Monte Carlo Method for Random Walk Problems*, 13th ed., Los Alamos Scientific Laboratory of the University of California, Los Alamos, December 1957.
- [27] P. Mendius, C. I. Harmon, R. Busch, J. Briesmeister, and R. Forster, “Criticality calculations with mcnp: A primer,” August 1994.
- [28] MATLAB, “The Mathworks, Inc.” Natick, Massachusetts. [Online]. Available: <https://nl.mathworks.com>
- [29] Ziegler, J.F., “SRIM: The Stopping Power and Range of Ions in Matter.” [Online]. Available: <http://www.srim.org>

## Appendix A The complete MCNPX input code

In this appendix the complete input file is shown that is used to obtain the radiographs in figure 11 and 14. In this report, not all details that are used in the code are explained. However, these can be looked up in the manual.

```

1-      MCNPX input code. 393216 voxels. 19.6mm phantom. CO.75.
2-      c -----
3-      c Cell specifications
4-      c -----
5-      c --- Aramica exit foil
6-          10 3 -1.44      10 -20 -30
7-      c --- 1st Collimator
8-          20 4 -8.515     40 -50 60 -70
9-      c --- 1st scatter foil
10-         30 5 -11.34     80 -90 -100
11-      c --- 2nd Collimator
12-         40 4 -8.515     110 -120 130 -140
13-      c --- 3th Collimator
14-         50 4 -8.515     150 -160 170 -180
15-      c --- 4th Collimator
16-         60 4 -8.515     190 -200 210 -220 230 -240 250
17-      c --- Field Collimator
18-         70 4 -8.515     260 -270 280 -281           $inner active part
19-         71 4 -8.515     260 -270 281 -290           $outer stopper part
20-      c --- Phantom
21-         80 6 -1.045     700 -710 730 -740           $solid water
22-         81 7 -1.823     700 -710 -730           $cortical bone
23-      c ----- Lanex screen lattice
24-      c --- Lanex screen
25-         200 0           800 -810 820 -830 840 -850   fill=2
26-      c --- Lanex screen voxel
27-         201 0           -870 860 -890 880 -910 900   u=2 lat=1 fill=6
28-      c --- Filling universe
29-         900 1 -7.34     990 -991 -992           u=6 $gadolinium
30-      c -----
31-      c --- Air (proton medium)
32-         998 2 -0.001205 996 -997 -998 &
33-                               #10 #20 #30 #40 #50 #60 #70 #71 #80 #81 #200
34-      c --- Void
35-         999 0           -996:997:998
36-      c --- CCCel
37-         9999 0          -9999
38-
39-      c -----
40-      c Surface specifications
41-      c -----
42-      c --- Aramica exit foil
43-         10   px  -0.0075           $Aramica exit foil us
44-         20   px   0               $Aramica exit foil ds
45-         30   cx   3               $Aramica exit foil radius
46-      c --- 1st Collimator
47-         40 1 px   0               $1st Collimator us
48-         50 1 px  1.6             $1st Collimator ds
49-         60 1 cx  1.0             $1st Collimator inner radius
50-         70 1 cx  4.0             $1st Collimator outer radius
51-      c --- 1st Scatter foil (various options 0.116 0.144)
52-         80 2 px   0               $1st Scatter foil us
53-         90 2 px  0.144           $1st Scatter foil ds
54-         100 2 cx  3.01           $1st Scatter foil radius
55-      c --- 2nd Collimator
56-         110 3 px  0               $2nd Collimator us

```

```

57-      120 3 px  5.5          $2nd Collimator ds
58-      130 3 cx  1.2          $2nd Collimator inner radius
59-      140 3 cx  3.0          $2nd Collimator outer radius
60-      c --- 3th Collimator
61-      150 4 px  0            $3th Collimator us
62-      160 4 px  7.0          $3th Collimator ds
63-      170 4 cx  2.25         $3th Collimator inner radius
64-      180 4 cx  5.0          $3th Collimator outer radius
65-      c --- 4th Collimator
66-      190 5 px  0            $4th Collimator us
67-      200 5 px  4.5          $4th Collimator ds
68-      210 5 py -20           $4th Collimator outer side
69-      220 5 py  20           $4th Collimator outer side
70-      230 5 pz -20           $4th Collimator outer side
71-      240 5 pz  20           $4th Collimator outer side
72-      250 5 cx  7.1          $4th Collimator inner radius
73-      c --- Field Collimator (various options)
74-      260 6 px  0            $Field Collimator us
75-      270 6 px  4.5          $Field Collimator ds
76-      280 6 cx  2.5          $Field Collimator inner radius
77-      281 6 cx  3.5          $Field Collimator skin, optional
78-      290 6 cx  12.5         $Field Collimator outer radius
79-      c --- Phantom with solid water and cortical bone
80-      700 7 px  0
81-      710 7 px  1.96         $Single slice
82-      720 7 px  3.92         $Double slice
83-      730 7 cx  1.5          $Inner radius
84-      740 7 cx  5            $Outer radius
85-      c --- Lanex screen (768*512)
86-      800 9 px  0
87-      810 9 px  0.01
88-      820 9 py -8.930232192
89-      830 9 py  8.930232192
90-      840 9 pz -5.953488128
91-      850 9 pz  5.953488128
92-      c --- Lanex screen voxel origin (0.023255813cm)
93-      860 9 px  0
94-      870 9 px  0.01
95-      880 9 py -8.930232192
96-      890 9 py -8.906976379
97-      900 9 pz -5.953488128
98-      910 9 pz -5.930232315
99-      c --- Filling universe for lanex screen
100-     990 9 px -1
101-     991 9 px  1
102-     992 9 cx  15
103-     c -----
104-     c --- Problem confinement
105-     996  px -2
106-     997  px 360
107-     998  cx 30                $radius void cylinder
108-     c --- Cookie cutter
109-     9999 cx  0.201
110-
111-     c -----
112-     c Coordinate transformations

```

```

113- c -----
114- c --- 1st Collimator
115-     TR1 1.9 0 0
116- c --- 1st Scatter foil
117-     TR2 9.8 0 0
118- c --- 2nd Collimator
119-     TR3 49.1 0 0
120- c --- 3th Collimator
121-     TR4 119.0 0 0
122- c --- 4th Collimator
123-     TR5 251.1 0 0
124- c --- Field Collimator
125-     TR6 310.1 0 0
126- c --- Phantom
127-     TR7 329.6 0 0
128- c --- Lanex screen and lanex voxels and filling universe lanex
129-     TR9 352.1 0 0
130- c -----
131- c Importance cards
132- c -----
133- c --- with sequence:
134- c Aramica exit foil                1
135- c 1st Collimator                    0
136- c 1st scatter foil                  1
137- c 2nd Collimator                    0
138- c 3th Collimator                    0
139- c 4th Collimator                    0
140- c Field collimator inner part       1
141- c Field collimator outer part       0
142- c Phantom solid water                1
143- c Phantom cortical bone              1
144- c Lanex screen                       1
145- c Lanex screen voxel                 1
146- c Filling universe                   1
147- c Air (proton medium)                1
148- c Void                               0
149- c CCCel                              0
150- c -----
151-     Imp:h  1 0 1 0 0 0 1 0 1 1 1 1 1 1 0 0
152-     Imp:n  1 0 1 0 0 0 1 0 1 1 1 1 1 1 0 0
153-     Imp:p  1 0 1 0 0 0 1 0 1 1 1 1 1 1 0 0
154-     Imp:e  1 0 1 0 0 0 1 0 1 1 1 1 1 1 0 0
155-     Imp:d  1 0 1 0 0 0 1 0 1 1 1 1 1 1 0 0
156-     Imp:t  1 0 1 0 0 0 1 0 1 1 1 1 1 1 0 0
157-     Imp:s  1 0 1 0 0 0 1 0 1 1 1 1 1 1 0 0
158-     Imp:a  1 0 1 0 0 0 1 0 1 1 1 1 1 1 0 0
159- c -----
160- c Mode specification
161- c -----
162-     Mode h n p e d t s a
163- c -----
164- c Physics specification
165- c -----
166-     Phys:h 200 0 -1 J 0 J 1
167-     Phys:n 200 0 0 -1 -1 0 1
168-     Phys:p 200 0 0 -1 1

```

```

169-      Phys:e 200 0 0 0 0 1 1 1 1 0
170-      Phys:d 200 3J 0
171-      Phys:t 200 3J 0
172-      Phys:s 200 3J 0
173-      Phys:a 200 3J 0
174-      Cut:h 2j 0
175-      Cut:d 2j 0
176-      Cut:t 2j 0
177-      Cut:s 2j 0
178-      Cut:a 2j 0
179-      c -----
180-      c Source definition proton beam
181-      c -----
182-      sdef x=-1 y=d1 z=d2 par=9 erg=d3 vec = 1 0 0 dir=1 & $ beam in x-dir
183-      ccc=9999
184-      sp1 -41 0.4 0          $ Int-spread in y-dir
185-      sp2 -41 0.4 0          $ Int-spread in z-dir
186-      si3 h 190.1 190.7      $ E-spread
187-      sp3 d 0 1
188-      c                      $ proton beam
189-      c -----
190-      c Specifications of tallies
191-      c -----
192-      prdmp 2j 1
193-      c -- 0.0005408328383
194-      F2:h (860<201[0:0 0:767 0:511]<200)
195-      FC2 proton flux through every voxel
196-      SD2 5.408328383 393215r          $area*10000
197-      *C2 0.75 0
198-      FQ2 C
199-      c --
200-      +F6 (201<201[0:0 0:767 0:511]<200)
201-      FC6 proton + secondary particle dose of every voxel
202-      SD6 3.96971E-5 393215r          $mass of voxel
203-      c -----
204-      c Material specifications
205-      c -----
206-      c -- Lanex (Gd202S)
207-      c -- density 7.34 g/cm3
208-      m1 64000 2
209-      8016 2
210-      16032 1          hlib=24h nlib=24c
211-      c -- Air
212-      c -- density 0.001205 g/cm3
213-      m2 7014 0.8
214-      8016 0.2 gas=1          hlib=24h nlib=24c
215-      c -- Aramica (modelled as Kevlar)
216-      c -- density 1.44 g/cm3
217-      m3 1001 10
218-      6012 14
219-      7014 2
220-      8016 2          hlib=24h nlib=24c
221-      c -- Copper (Model for Brass)
222-      c -- density 8.515 g/cm3
223-      m4 29063 0.6917
224-      29065 0.3083          hlib=24h nlib=24c

```

```

225-      c -- Lead
226-      c -- density 11.34 g/cm3
227-          m5      82206   0.241
228-              82207   0.221
229-              82208   0.524          hlib=24h  nlib=60c
230-      c -- Solid Water
231-      c -- density 1.045 g/cm3
232-          m6      1001    8.02
233-              6012   67.22
234-              7014    2.41
235-              8016   19.91
236-              17035   0.14
237-              20040   2.31          hlib=24h  nlib=24c
238-      c -- Cortical Bone
239-      c -- density 1.823 g/cm3
240-          m7      1001    3.41
241-              6012   31.41
242-              7014    1.84
243-              8016   36.5
244-              17035   0.04
245-              20040   26.81          hlib=24h  nlib=24c
246-      c ---
247-          nps 2000000000
248-          ctme 3000

```

## Appendix B MATLAB code to import the F2 tally with the experimental data

In this appendix the complete MATLAB code is given that has been used to import the data from the F2 tally of the MCNPX output file and to import the data that has been obtained from the experiment. A radiograph is obtained by ordering the data values in a specific way. In this code, the data that has been obtained from the experiment has been divided by the data of the F2 tally. In this way, the radiograph of the experiment has been corrected for multiple Coulomb scattered protons. If a percentage sign has been put in front of the line, MATLAB does not read that line. Details about the code can be looked up in the manual.

```

% IMPORT DATA SETS OF REJECTION OF PROTON FLUX (F2 TALLY)
% FROM RADIOGRAPH OBTAINED BY THE EXPERIMENT (393216 VOXELS)

```

```

% This code assumes that the origin voxel starts at the bottom left of the
% scintillation screen. The screen is filled starting from the bottom row
% to the top row, while filling from minus y to plus y.

```

```

clear all
%%%%%%%%%%%%%%%%%%%%%%%%%%%%%%%%%%%%%%%%%%%%%%%%%%%%%%%%%%%%%%%%%%%%%%%%
% data from F2
%%%%%%%%%%%%%%%%%%%%%%%%%%%%%%%%%%%%%%%%%%%%%%%%%%%%%%%%%%%%%%%%%%%%%%%%
A = importdata('jel6_f2.txt');

```

```

% bin 1 and bin 2 are scattered and not scattered protons, respectively.
bin1 = A(:, [1,5]);
bin2 = A(:, [3,7]);

```

```

% Scattered and straight are column vectors of the scattered protons
% and not scattered protons, respectively.
scattered = reshape(bin1', [], 1);
straight = reshape(bin2', [], 1);
total = scattered + straight;

B = 1./straight;
B(straight==0) = 0;

%%%%%%%%%%%%%%
% data from experiment
%%%%%%%%%%%%%%
C = fitsread('Background.fit');
D = fitsread('Contrast_Phantom_1disk_1MMU-001.fit');

% Rejecting background noise
E = minus(D,C);

% Align the radiograph obtained by the experiment with the
% radiograph obtained by the simulation.
F = circshift(E, [18 764]);

% Correct the radiograph obtained by the experiment for the non-constant
% flux in front of the scintillation screen
G = reshape(F', [], 1);
valuesStraight = B.*G;

% Order the data so that it ends up at
% the correct voxel of the screen.
H = reshape(valuesStraight, 768, 512);
I = H';

% Normalizing the data points by dividing by the sum of all data.
J = sum(I(:));
invJ = 1/J;
K = invJ*I;

% Reduce high peaks in the data
L = medfilt2(K);

% Plotting cross section of the energy deposition versus voxel column number,
% averaging over voxel row number 251 to 260.
figure
M = L(251:260, :);
N = mean(M);
plot(N')

% Plotting the radiograph
x=linspace(0,768,769);
y=linspace(0,512,513);

i = imagesc(x,y,L);

colorbar;
set(gca, 'YDir', 'normal');
oldcmap = colormap(gray);

```

```
colormap(flipud(oldcmap));
caxis([0 0.000035]);
```

## Appendix C MATLAB code to import the F6 tally

In this appendix the complete MATLAB code is given that has been used to import the data from the F6 tally of the MCNPX output file. A radiograph is obtained by ordering the data values in a specific way. If a percentage sign has been put in front of the line, MATLAB does not read that line.

```
% IMPORT DATA SETS OF ENERGY DEPOSITION (F6 TALLY) FOR 393216 VOXELS

% This code assumes that the origin voxel starts at the bottom left of the
% scintillation screen. The screen is filled starting from the bottom row
% to the top row, while filling from minus y to plus y.

clear all
A = importdata('jel2_f6.txt');

% Values and errors are column vectors of the
% data and corresponding errors, respectively.
B = A';
C = reshape(B, [], 1);
values=C(1:2:end,:);
errors=C(2:2:end,:);

% Order all values and errors so that they end up at
% the correct voxels of the screen.
D = reshape(values, 768, 512);
E = D';
F = reshape(errors, 768, 512);
G = F';

% Normalizing the data points by dividing by the sum of all data.
% Errors don't have to be normalized.
H = sum(E(:));
invH = 1/H;
I = invH*E;

% Reduce high peaks in the data
J = medfilt2(I);

% Plotting cross section of the energy deposition versus voxel column number,
% averaging over voxel row number 251 to 260.
figure
K = J(251:260,:);
L = mean(K);
plot(L');

% Plotting the radiograph
x=linspace(0, 768, 769);
y=linspace(0, 512, 513);

i = imagesc(x, y, J);
```

```
colorbar;  
set(gca,'YDir','normal');  
oldcmap = colormap(gray);  
colormap(flipud(oldcmap));  
caxis([0 0.000035]);
```